ECOLE POLYTECHNIQUE FÉDÉRALE LAUSANNE
CENTER FOR RESEARCH IN PLASMA PHYSICS • SUPERCONDUCTIVITY

LRP 775/03 **December 2003**

Analysis and interpretation of Tcs measurements of the TFCI experiment

Final Report

(EFDA Task TM-005.G1-Magnet_M12, Deliverable #7)

Claudio Marinucci

CRPP • SUPERCONDUCTIVITY
CH-5232 VILLIGEN PSI
SWITZERLAND

Abstract—The toroidal Field Conductor Insert (TFCI) coil was tested at 46 kA in the 13 T background magnetic field generated by the Central Solenoid Model Coil. The single layer TFCI coil uses a Nb_3Sn cable-in-conduit conductor in a Titanium jacket. The object of this work is to verify the data self-consistency, and to apply a thermal, hydraulic and electrical simulation to derive the strand performance in the cable. We present the results of the analysis in support of the interpretation of a subset of current sharing temperature measurements. After estimation of the n-value in the voltage-current equation, we perform the simulations using the total longitudinal strain as the only fitting parameter; the resulting value is much larger than the value expected from simple thermal contraction considerations.

Table of contents

1. Introduction

The ITER Toroidal Field Conductor Insert (TFCI) coil was developed and built by a collaboration of Russian scientific and industrial institutions to simulate the conductor performance under the ITER TF conditions, and to confirm the validity of design and fabrication techniques of the ITER superconducting magnets. The TFCI was charged without training in the background field of the ITER Central Solenoid Model Coil (CSMC) test facility at the Japan Atomic Energy Research Institute in Naka, Japan, to the design current of 46 kA at the peak magnetic field of 13 T.

One of the objectives of the TFCI tests was to measure the current sharing temperature (T_{cs}) behavior of the conductor and to compare it with predictions based on strand measurements. In general this comparison implies the deduction of the strand performance in the cable; this requires iterations with the thermal hydraulic simulations to provide approximated performance values for the strand in the cable which fit thermal and voltage data.

Although the TFCI met the design objectives, it also showed results which require further studies [1]. Goal of this analysis is to derive the strand performance in the cable by simulating the temperature profile along the conductor length. A comparison with measurements is problematic since the response of the distributed temperature sensors has shown some inconsistency, probably due to an unknown magnetic field sensitivity of the temperature sensors.

The analysis has focused on 8 experimental Tcs runs in a broad range of operating conditions, e.g. 17-46 kA for the TFCI current and 5-12 T for the CSMC background magnetic field. The major characteristics of these Tcs tests are summarized in Table 1. The experimental data acquisition system (DAS) signals used in this analysis are listed in Table 2. Our preliminary analysis has assessed the consistency of the experimental data and has defined the strategy to be used in the simulation model.

Details of this work are presented in Appendices, resulting in some duplication with the main text.

This activity started in February 2003 and is completed by this Final Report.

2. Description of the TFCI

The TF Insert is a one-layer solenoid with 9 turns, connected to superconducting bus bars at the lower and upper terminal joints. It features a Nb_3Sn dual channel cable-in-conduit conductor (CICC) with thin wall conduit. The conduit if made of titanium with low coefficient of thermal expansion: the goal is to minimize the degradation of the strand properties by reducing the thermal strains in the CICC. The preformed and heat treated CICC is embedded in a stainless steel mandrel.

The coil is cooled in parallel with the CSMC by forced-flow of supercritical helium (SHe) at 4.5 K and 0.6 MPa. The SHe flows from the lower to the upper joint, which are approximately 5 m apart in the vertical direction. The mandrel and the joints are cooled by separate circuits at 4.5 K (Fig. 1).

The TFCI conductor consists of 1152 Nb_3Sn strands (3 x 4 x 4 x 4 x 6). The last-but-one 6 sub stages are twisted around a spiral central channel (manufactured by SHOWA). The helium flows in two regions: in the central channel and in the voids

around the strands (the bundle region). The conductor is insulated with glass tape, impregnated with epoxy resins and cured. The length of the TFCI conductor is approximately 43 m.

The TFCI is instrumented with voltage taps and thermometers along the conductor length, as well as with pressure, temperature and mass flow rate (dm/dt) sensors at the two ends near the terminal joints. During the Tcs runs the helium inlet temperature is slowly ramped by means of a resistive heater located upstream of the lower joint (Fig. 2). The thermometers before the lower joint (at inlet) and after the upper joint (at outlet) provide reliable signals, as it is the case with the voltage taps. By contrast, as mentioned above, a comparison with measurements of the distributed temperature sensors is problematic.

Details of the TFCI conductor and coil are given in [2].

3. Preliminary analysis

Goal of the preliminary analysis is to assess the consistency of the experimental data and to define the resulting strategy to be used in the definition of the TFCI simulation model described below. In particular, we have investigated the pressure drop correction and the heat exchange at mandrel and joints.

- The helium inlet temperature (T_{in}), the inlet pressure (p_{in}) and the outlet pressure (p_{out}) are needed as thermal hydraulic boundary conditions (BC's) to calculate the mass flow rate in the simulation code THEA (see below). The experimental signal ITF_TC_IN and ITF_PT_IN are used in the simulation as reliable BC's for T_{in} and p_{in}, respectively. The raw outlet pressure signal ITF_PT_OUT cannot be used as BC in the simulation model. The outlet pressure used in the simulation is p_{out} = ITF_PT_IN - C3, where the correction factor C3 (4800 Pa < C3 < 5800 Pa, dependent on the operating conditions) includes the gravity correction as well as other unidentified effects. The resulting correlation is in agreement with the TFCI pressure drop performance [3,4].
- The TFCI winding is in good thermal contact with mandrel and joints, i.e. coil components which are independently cooled at ~4.5 K. The analysis of the heat exchange between TFCI and these components shows that the characteristic parameter p*h (i.e. Q=p*h*ΔT, where p is the exchange perimeter, h is the heat transfer coefficient and ΔT is the temperature difference between TFCI and mandrel/joints) is approximately 8 W/K for the each joint and considerably lower than 1 W/K for the mandrel. The latter is set to zero in the simulations.

Details of this preliminary analysis are given in Appendix A.

4. THEA model

The coupled thermal, hydraulic and electrical analysis is performed with the code THEA™ by CryoSoft [5]. The code was validated in the SeCRETS and CONDOPT experiment performed in the SULTAN test facility [6,7].

We consider the last-but-one cable stage, modeling the CICC as 6 twisted super strands (petals) with uniform properties.The resulting model of the conductor cross section includes (Fig. 3):

- 9 thermal components, i.e. 6 super strands including Nb_3Sn and Cu (T1-T6) + Titanium spiral (T7)+ Titanium jacket (T8) + insulation (T9),
- 2 hydraulic components, i.e. bundle (H1) and spiral central channel (H2), and
- 6 electric components (E1-E6), i.e. 6 super strands.

Each component has a set of independent variables, i.e. current in the electric components and temperature in the thermal components.

Details of the THEA™ model are given in Appendix B.

4.1. Thermal hydraulic model

The total length of the thermal hydraulic model is 49.3 m; this includes the winding in the mandrel, the lower and upper 'tails', joints and pipes (Fig. 2). The super strands are thermally coupled through a small thermal resistance and are cooled by helium flow through heat transfer at the wetted perimeter. We use the Katheder correlation without correction factor, and the CEA correlation [8] to characterize the friction factor of the bundle and the SHOWA spiral, respectively. The choice of neglecting the bundle correction factor is motivated by the very limited sensitivity of the overall results to a variation of this parameter in the range 1 - 3 (the ITER CICC vlaue is ~ 2).

As mentioned, thermal hydraulic boundary conditions are the measured He temperature at inlet, and He pressure at inlet and outlet; the gravity correction is added to the latter to fit the pressure drop correlation.

4.2. Strand and electrical model

The Nb_3Sn strand for the TF Insert was fabricated by Bochvar Institute of Inorganic Materials, Moscow, Russian Federation. Extensive measurements of the strands showed a relatively low scatter of properties. The critical current I_c was measured on several samples, which underwent different fabrication steps. The non copper critical current density J_c (at 12 T and 4.2 K) of strands from different batches varied from 550 to 650 A/mm^2 and more than 80% fell within 570-630 A/mm^2; the corresponding n-value of the strand is ~ 30 [1].

The Nb_3Sn strand is characterized by the Summers scaling parameters:

- $T_{c0m} = 17.0$ K
- $B_{c20m} = 34.0$ T
- $C_0 = 7.1 \times 10^9$ $AT^{0.5}m^{-2}$.

T_{c0m} and B_{c20m} are derived from measurements of strand #94 assuming a longitudinal strain of -0.25%, and C_0 is scaled up to fit the mean value of strands in the cable [9].

Each super strands is electrically coupled through mutual inductances and inter strand conduction (~0.32 $MS/m = 1/R_c$, where $R_c = 3.15$ $\mu\Omega$m is the average interpetal contact resistance of the ITER CS1.1/CS2 conductors after transverse cyclic loading [10]), and is characterized by the non-linear voltage current equation $E=E_0(I/I_0)^n$. The cable n-values are given below.

Heat generation in the lower/upper joints is accounted for by using a constant electrical resistance R_{joint} = 2 nΩ (see also Appendix A).

4.3. Magnetic field

Detailed calculations of the TFCI magnetic field were performed in support of the TFCI test program. The total magnetic field, constant in the cross section of each of the 6 super strands, is obtained by adding the CSMS external field and the self field at the center of each last-but-one cable stage (the twist pitch is 407 mm). The '9-turn model' results are used to prepare the distribution of the total field, per unit of CSMC and TFCI current, as a function of the conductor length. This distribution is then fed to the THEA™ model. A higher field accuracy, which could be obtained using a second-last-but-one model with 4x6 super strands, is beyond the scope of this study. This would generate a considerable increase of model complexity and CPU time.

The electrical connections at the cable beginning and end are assumed to be symmetrical, i.e. same current in each super strand.

4.4. Cable n-values

The cable n-values are estimated from the resistive voltage signals, using simplifying assumptions necessary since Tcs runs are performed at constant current. The resulting TFCI cable n-values are in the range between 6 (at 17 kA) and 12 (at 46 kA). The corresponding n-values of the strand are in the range between ~13 (at 17 kA) and ~20 (at 46 kA). Details of the estimation of the cable n-values are given in Appendix G.

4.5. Simulation parameters

We use 500 nodes along the conductor length for the standard simulation, and 2000 nodes for the special case. The finer discretization allows to better appreciate the distribution of interesting parameters along the one-dimensional nodal coordinate X but has only a negligible effect on the numerical results.

5. Simulations with the code THEA™

5.1. Strategy

We first tune for each T_{cs} run the pressure drop correction factor C3 in order to match the experimental outlet mass flow rate.

Having derived for each T_{cs} run the upper and lower n-values based on measured resistive voltages, the only fitting parameter in the simulations is ε. This variable does not have a defined physical meaning; it can be regarded as a cable global quantity including the contributions of bending strain, thermal strain, electromagnetic loading and other unidentified degrading effects, and is kept constant during the run. We start the iterative process from the arbitrary reference value of -0.25% and decrease it (i.e. larger negative number) until the simulated resistive voltage V0304 is in agreement with the experimental data, at the exact time when the experimental take off takes place. The voltage V0304 is taken over approximately 4.5 m of conduc-

tor length near X ~ 35 m. The selection of V0304 is motivated by the fact that it exceeds other voltages at take off time in all T_{cs} runs, with few exceptions.

We apply the above procedure for the upper and lower n-values, and also for n-values outside this range, until the 'optimal' solution is found, i.e. best comparison of outlet temperature and V0304 voltage.

Simulated and experimental thermal hydraulic and electric signals are compared a posteriori. The list of investigated runs is given in Table 1.

5.2. Results of run #44-2

The typical run #44-2 is performed at high magnetic field (B_{max} = 12.16 T) and high TFCI current (46 kA); the take off time at the end of the run is t_{end} = 6199 s. Using the combination of n = 9.3 and ε = -0.60%, simulated and measured results are in acceptable agreement during the complete evolution. For example, at t_{end} the resistive voltage error varies between a maximum of ~ 0.6 mV at V0809 and a minimum, of less than 0.2 mV at V0304, with smaller errors before current sharing (t < 5000 s) (Fig. 4). The errors of temperature and mass flow rate at outlet are smaller than 0.2 K (Fig. 5) and smaller than 0.2 g/s, respectively. Control over mass flow rate is possible through the pressure correction factor C3.

The simulated results along the conductor length provide a virtual instrument for the interpretation of the experiment, e.g. the quantitative assessment of variables which cannot be measured by the lack of sensors, or which can be measured but whose signals are not reliable (as in the case of the TFCI distributed temperature sensors). Fig. 6 and 7 show the snapshot of run #44-2 at t_{end}. The temperature has a parabolic increase from lower to upper end of the winding (3.5 m < X < 45.8 m) while elsewhere the drop of temperature is driven by the heat exchange in the joints. The temperature is not homogenous in the conductor cross section, i.e. the peak value is ~ 8.05 K in the super strands T5 and T6 (X = 42.7 m) and the difference to other super strands is ~ 0.15 K. The amount of current sharing is limited to ~ 300 A. Shortly after t_{end} (+ 1s) the take off is fully developed, the conductor temperature is ~ 50 K and current is shared between super strand T5-T6 (~ 3 kA each) and T1-T2 (~ 12 kA each). The asymmetric temperature distribution in the conductor cross section is a simulation artefact occurring although the simulation model is fully symmetrical, e.g. ideal electrical joint properties, conductor cross section properties, etc.

Details results of run #44-2 are given in Appendix C.

5.3. Results of the other Tcs runs

In other T_{cs} runs the simulated results are qualitatively similar to the results of run #44-2.

The selected pressure correction factor varies in the range 4800 Pa < C3 < 5800 Pa. Depending on the operating conditions, the 'optimal' n-value varies between 7.6 and 10.2 and the current sharing temperature between 7.04 K and 9.06 K. These results of T_{cs} are close to those obtained from measured resistive voltages (Appendix G).The resulting fitting parameter is approximately -0.60% and independent of the electromagnetic load, in agreement with [11].

The simulation of runs #57-3 and #85-3 is problematic because of (a) premature quenches when using realistic n-values, even at zero strain, or (b) very large underestimation of the resistive voltages when using unrealistically low n-values. These two runs were performed at low magnetic field (~ 5 T) and high temperature (~ 9 K at the beginning of the run). We believe that the discrepancy may be due to the fact that the scaling parameters for the critical current fit have been determined in a range of temperature (~ 4.5 K) and field (~ 11 T) which is far from the conditions simulated. The optimization of the Summers parameters in the complete range of operating conditions of the Tcs runs is beyond the scope of this study.

A summary is shown in Table 3. Details are given in Appendix D.

5.4. Sensitivity studies

A limited sensitivity analysis is performed to assess the influence of two input parameters on the relevant results of the simulation:, i.e.

- pressure factor correction: in the range 5800 Pa < C3 < 6800 Pa (see Appendix E) and
- n-Value: in the range between upper and lower n-values assessed through the experimental voltages (see Appendix F).

The study, applied to three runs at high magnetic field (> 11.4 T) and low (17.6 kA), medium (31.0 kA) and high TFCI current (46.0 kA) shows that in the investigated range the output variables are insensitive to variation of C3 and n-value, and the 'best' total strain results in larger negative values for lower C3 and lower n-values.

6. Summary

A subset of TFCI current sharing temperature experiments has been analyzed with a thermal, hydraulic and electrical simulation model.

- An acceptable agreement of simulated and measured results is achieved if the fitting parameter ε (including all strain and degradation) is approximately -0.60% and independent of electromagnetic load. This result confirms a former analysis. For comparison, the expected thermal strain at zero loading in conductors with titanium jacket is less than -0.30%.
- This analysis has shown that the n-value (7.6 - 10.2) and T_{cs} (7.0 - 9.1 K) of the CICC are considerably lower than the respective values measured from the strand ($13 < n < 20$ and $8.4 < T_{cs} < 10.2$). A change of strand intrinsic properties, e.g. some factors in fabrication, cool down or electromagnetic loading is responsible for the reduction of the critical current of individual strand, and their n-value.
- Due to the above unidentified degradation of the CICC, it is not possible to describe the strands in the cable by the Summers equation for the original strands (an optimization for the Summers parameters is beyond the scope of this study).

7. Acknowledgements

This work was performed in the frame of the EFDA Task M12 within the European Fusion Technology Program. The author is grateful to Denis Bessette (ITER), Neal Mitchel (ITER), Nicolai Martovetsky (LLNL), Luca Bottura (CERN), Boris Stepanov (CRPP), Rainer Wesche (CRPP), Pierluigi Bruzzone (CRPP) for fruitful discussion, to Yoshi Takahashi (JAERI) for experimental data, and to Kumar Padyiath (PSI) for computer support.

8. References

1. N. Martovetsky, M. Takayasu, J. Minervini, et al., 'Test of the ITER TF Insert and Central Solenoid Model Coil', IEEE Trans. App. Supercond., 13,2:1441-1446, 2003
2. N. Cheverev, V. Glukhikh, O. Filatov, et al., 'ITER TF Conductor Insert coil manufacture', IEEE Trans. App. Supercond. 12, 1:548-551, 2002
3. K. Hamada, T. Kato, K. Kavwano, et.al., 'Pressure drop performance of the ITER TF conductor insert', accepted for publication in the proceedings of ICEC-19
4. K. Hamada, private communication, Nov. 2003
5. L. Bottura, C. Rosso, M. Breschi, 'A general model for thermal hydraulic and electric analysis of superconducting cables', Cryogenics 40, 617-626, 2000
6. C. Marinucci, L. Bottura, P. Bruzzone, 'Application of the code THEA to the CONDOPT experiment in SULTAN', IEEE Trans. Appl. Supercond. 12, 1:1524-1527, 2002
7. L. Bottura, C. Marinucci, P. Bruzzone, 'Analysis of current redistribution in a Cable-in-Conduit-Conductor', accepted for publication in the proceedings of CEC/ICMC 2003
8. S. Nicollet et.al., 'Hydraulics of the ITER Toroidal Field Model Coil Cable-in-Conduit Conductor', Proc. Int'al Symp. of Fusion Technology-98, 771-774, 1998
9. D. Bessette, ITER International Team Garching, Germany, private communication, June 2003
10. A. Nijhuis et.al., 'Electromagnetic and mechanical characterisation of ITER CS-MC conductors affected by transverse cycling loading. Part 2: interstrand contact resistances', IEEE Trans. Appl. Supercond. 9, 2:754-757, 1999
11. L. Zani, S. Egorov, 'Electromagnetic analysis of the ITER Toroidal Field Coil Insert properties', IEEE Trans. Appl. Supercond. 13, 2:1416-1419, 2003
12. 'Cable Interactive Designer (CID)', CryoSoft User's Manual, Ver. 1.0, 2002

Run #	I_{CSMC} (kA)	I_{TFCI} (kA)	B_{max} (T)
40-3	40.140	31.775	11.511
43-3	40.842	17.609	11.475
44-2	41.663	46.030	12.158
52-3	34.927	34.329	10.124
57-3	16.077	46.060	5.147
63-2	40.814	17.682	11.469
68-2	40.832	17.685	11.474
85-3	16.070	46.085	5.146

Table 1. List of T_{cs} runs investigated

File name (run_xxx_)	DAS signal	Description of the signal
384	ITF_TC_IN	conductor temperature at inlet
	ITF_PT_IN	conductor pressure at inlet
	ITF_TC_OUT	conductor temperature at outlet
	ITF_PT_OUT	conductor pressure at outlet
	ITF_PD_ALL	conductor differential pressure (inlet /outlet)
	CSV_TC_TB-CS1E	busbar temperature at inlet
	CSV_PT_PI-CS1E	busbar pressure at inlet
	CSV_TC_TC_STR1E	mandrel cooling pipe temperature at inlet
	CSV_PT_PI_STR1E	mandrel cooling pipe pressure at inlet
	ITF_VD_JT	voltage drop at upper terminal joint
	ITF_VD_JB	voltage drop at lower terminal joint
384vt	ITF_FCT_INc	conductor mass flow rate at inlet
	ITF_FCT_OUT	conductor mass flow rate at outlet
	ITF_FCT_STR-IN	mandrel cooling circuit mass flow rate
	SCB_FCT_IPIc	upper busbar mass flow rate
	SCB_FCT_INIc	lower busbar mass flow rate
64	ITF_VD_0203	voltage tap E0203
	ITF_VD_0304	voltage tap E0304
	ITF_VD_0405	voltage tap E0405
	ITF_VD_0506	voltage tap E0506
	ITF_VD_0607	voltage tap E0607
	ITF_VD_0708	voltage tap E0708
	ITF_VD_0809	voltage tap E0809
	ITF_VD_0910	voltage tap E0910

Table 2. Data Acquisition System signals used in the study

Run #	B_{max} (T)	I_{TFCI} (kA)	BI (kN/m)	t_{end} (s)	C3 (Pa)	n (-)	ε (%)	T_{cs} (K)
Note								(c)
40-3	11.511	31.775	365.8	5267 (a)	5800	8.6	-0.5840	8.25 (8.46)
43-3	11.475	17.609	202.1	4567	5800	7.6	-0.5905	9.05 (n.a.)
44-2	12.158	46.030	559.6	6199	5800	9.3	-0.5995	7.04 (7.28)
52-3	10.124	34.329	347.5	3581	4800	10.2	-0.5850	8.95 (9.25)
57-3	5.147	46.060	237.1	4284	(b)	(b)	(b)	n.a. (11.72)
63-2	11.469	17.682	202.8	7532	5000	7.6	-0.5875	9.06 (n.a.)
68-2	11.474	17.685	202.9	4453	5300	7.6	-0.5891	9.05 (n.a.)
85-3	5.146	46.085	237.2	5745	(b)	(b)	(b)	n.a. (11.62)

(a) the simulation t = 0 s corresponds to the experimental t = 700 s.
(b) the simulation is not reliable with the given strand data because of either premature quench when using realistic n-values (even at ε = 0), or because of very large underestimation of the resistive voltages when using unrealistically low n-values
(c) at B=B_max. In parenthesis are the values obtained with the method described in Appendix G

Table 3. Operating conditions and summary of simulation results using the optimal combination of n-value and fitting parameter. Data ε and T_{cs} are computed results, other data are input parameters. For comparison, the corresponding n-values of the strand are in the range between 13 (at 17.6 kA) and 20 (at 20 kA).

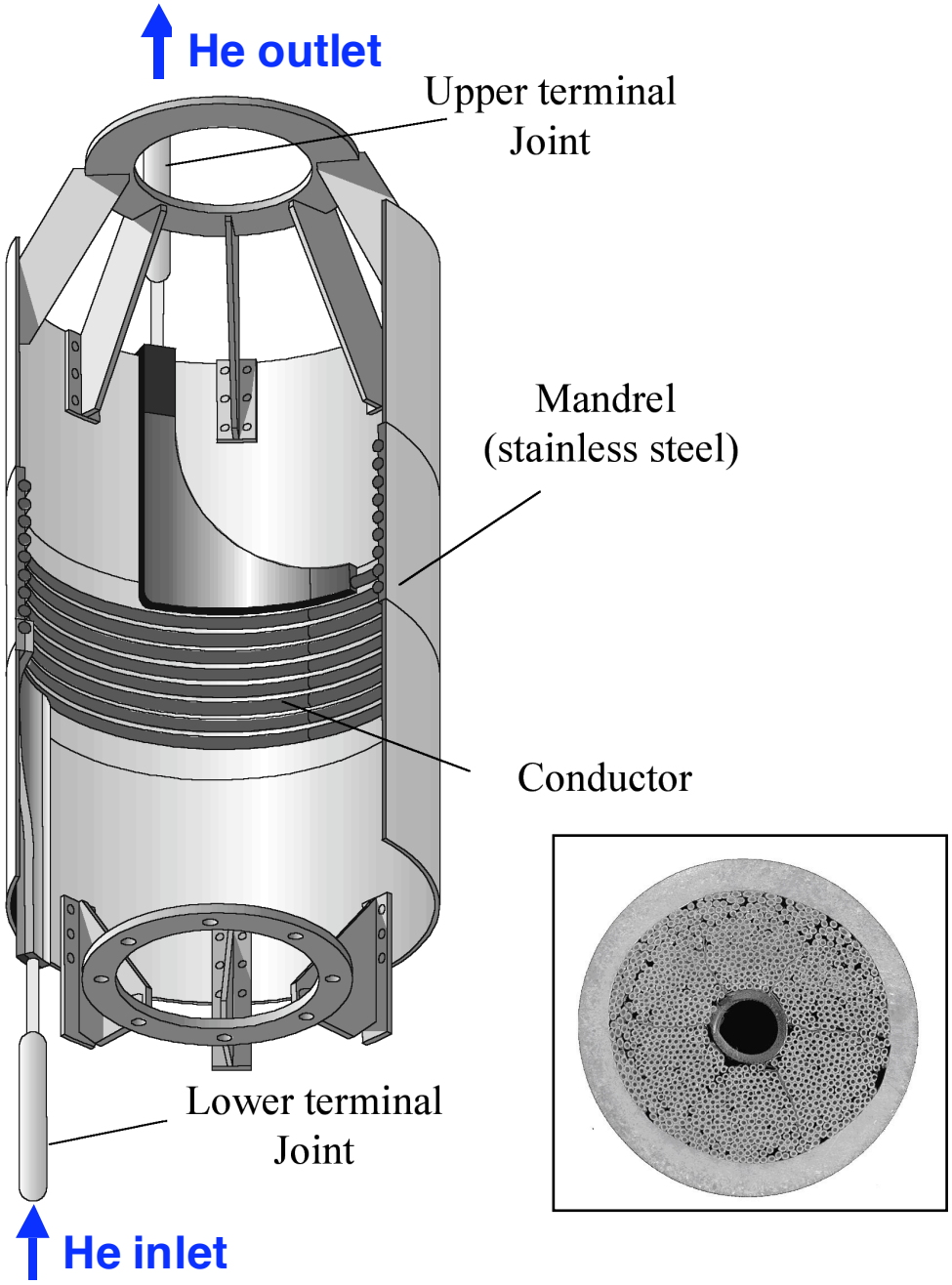

Figure 1. Global view of the TFCI (left). The helium inlet is at the lower terminal joint and the helium outlet at the upper terminal joint. Cross section of the Nb3Sn dual channel CICC used for TFCI (right). Both photos are courtesy of CEA.

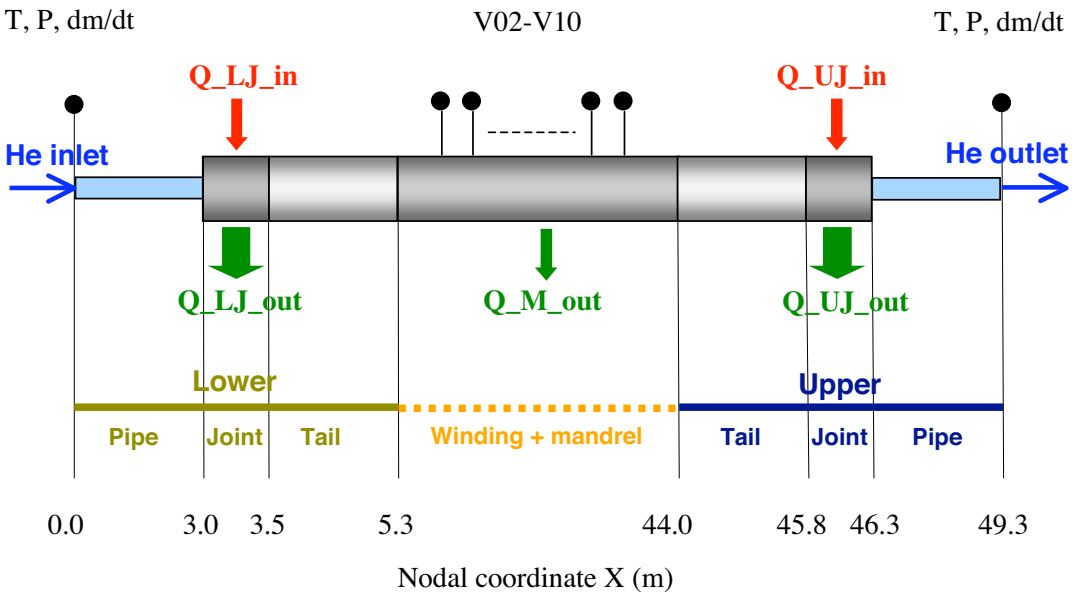

Figure 2. One-dimensional simulation model of the TFCI. Q_in is the heat generated and Q_out is the heat absorbed. The black dots are the sensors of the Data Acquisition System.

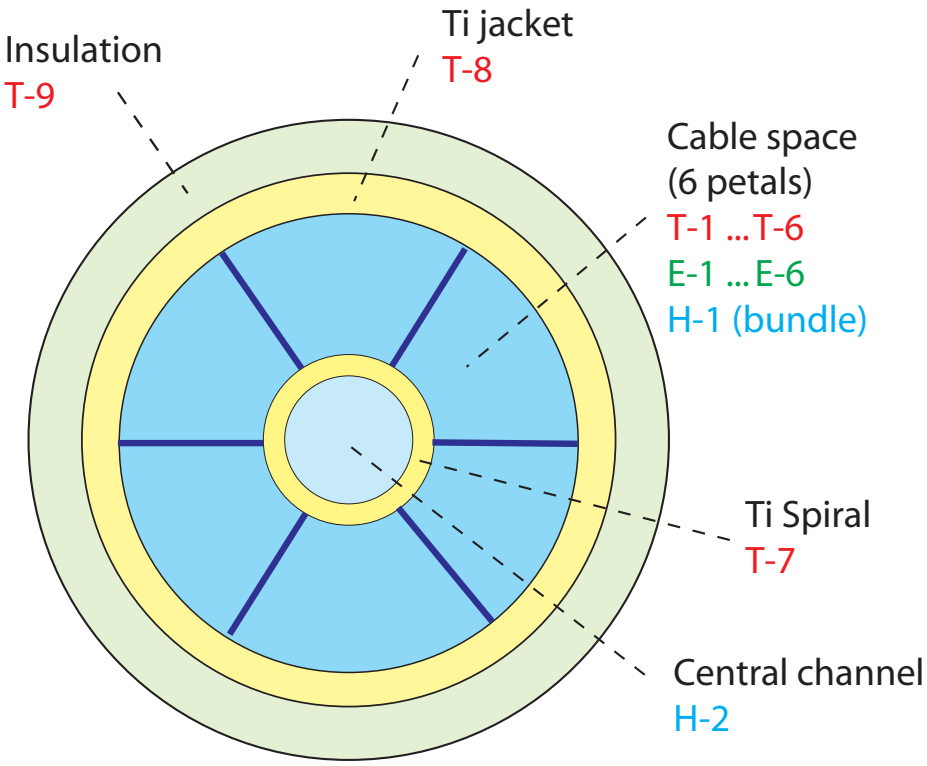

Figure 3. Model of the TFCI Nb_3Sn dual channel CICC used in the simulation with the code THEA™.

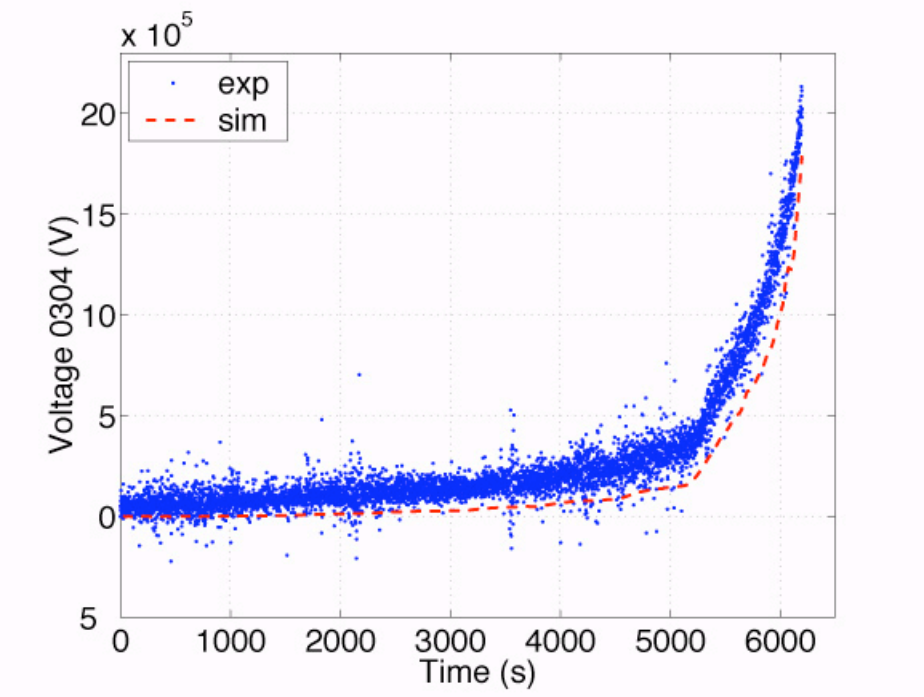

Figure 4. Time history of the resistive voltage V0304 (run # 44-2). Comparison of experimental (blue) and simulated (red) results.

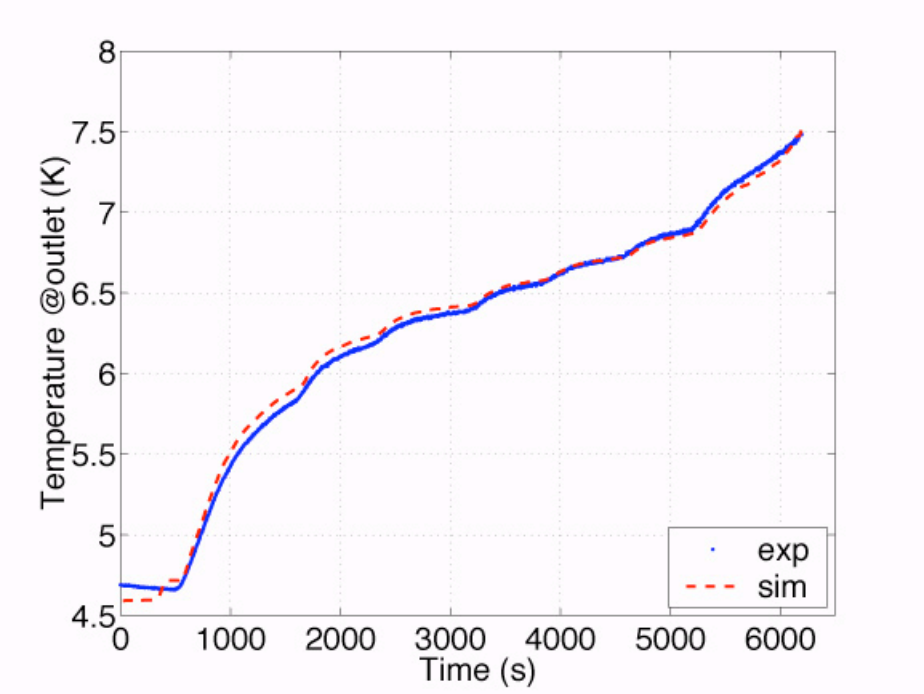

Figure 5. Time history of the helium temperature at outlet (run # 44-2). Comparison of experimental (blue) and simulated (red) results.

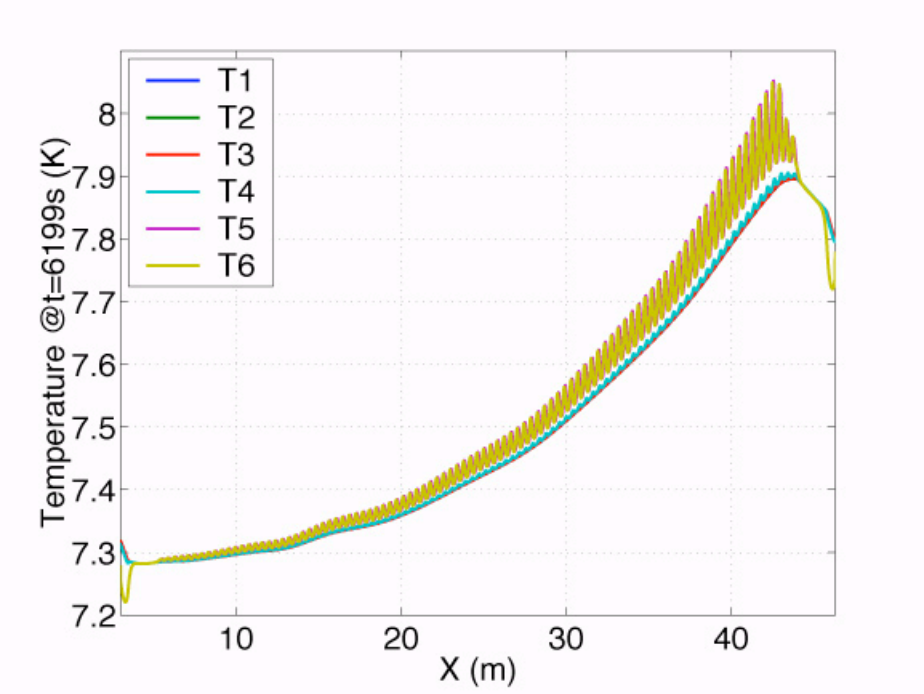

Figure 6. Simulated distribution of the conductor temperature in the 6 super strands along the conductor length, at the end of run #44-2. The thermal oscillations have approximately the same periodicity of the self field, i.e. the thermal time constant appears to be negligible. The asymmetric temperature distribution in the conductor cross section is a simulation artefact occurring although the simulation model is fully symmetrical, e.g. ideal electrical joint properties, conductor cross section properties, etc.

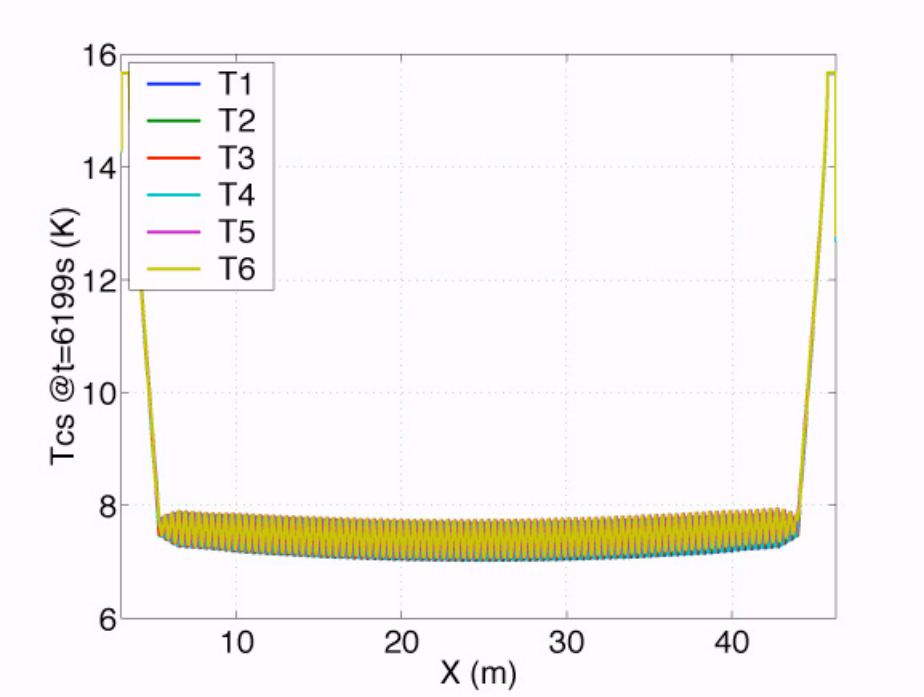

Figure 7. Simulated distribution of the current sharing temperature in the 6 super strands along the conduct length, at the end of run #44-2. The periodicity is due to the self field effect.

This page is left intentionally blank.

Appendix A. Preliminary analysis

A.1. Pressure drop correction

The helium inlet temperature (T_{in}), the inlet pressure (p_{in}) and the outlet pressure (p_{out}) are needed as thermal hydraulic boundary conditions (BC's) to calculate the mass flow rate in the simulation code THEA™.

The experimental signal ITF_TC_IN and ITF_PT_IN can be used in the simulation as reliable BC's for T_{in} and p_{in}, respectively, whereas the outlet pressure signal ITF_PT_OUT appears to be inconsistent. A detailed list of experimental signals is shown in Table 2. By plotting the differential pressure Δp vs. dm/dt for all runs investigated, as

- Δp = ITF_PT_IN - ITF_PT_OUT, i.e. the difference of the raw pressure signals at inlet and outlet, and
- Δp = TF_PD_ALL, i.e. the experimental differential pressure signal,

both variables Δp show a large offset when extrapolated to $dm/dt=0$ (Fig. A1). This offset can be due to a variety of reasons, e.g. sensor displacement in the vertical direction (~5 m), sensor precision, etc.

For comparison we also show in Fig. A1 the theoretical curve obtained by using the TFCI thermal hydraulic model at constant temperature (4.5 K) in the THEA™ code, i.e. the SHOWA correlation to characterize the friction factor of the spiral central channel, and the Katherder correlation to characterize the friction factor of the bundle. The resulting theoretical curve is in agreement with the TFCI pressure drop performance by Hamada [3,4].

To match the TFCI theoretical curve, the outlet pressure to be used in the simulation p_{out} is approximated with the following three corrections:

- correction #1
  - p_{out} = ITF_PT_OUT + C1,
  - with C1 = ~7500 Pa = constant
- correction #2
  - p_{out} = ITF_PT_IN - TF_PD_ALL + C2,
  - with C2 = ~3900 Pa = constant
- correction #3
  - p_{out} = ITF_PT_IN - C3,
  - with 4800 Pa < C3 < 5800 Pa, dependent on the operating conditions.

Correction #3 is used for all simulations because it provides the best match between simulated and experimental helium mass flow rate at the outlet (dm/dt_out). In contrast, the two former and more 'physical' corrections #1 and #2 give a systematic overestimation of dm/dt_out in the first 1/4 of the run, while giving a good match in the final 3/4 of the run. There is no plausible explanation for this results and more work is necessary to gain a better understanding.

The effect of a variation of the pressure drop correction C3 on the simulated results of all T_{cs} runs is negligible, as shown by a sensitivity study described in Appendix F.

A.2. Heat exchange at mandrel and joints

The TFCI winding is in good thermal contact with the lower joint, the mandrel and the upper joint, three coil components which are independently cooled at ~4.5 K. Goal of this analysis is to asses the order of magnitude, i.e. to obtain an approximated and sustainable model, of the heat exchange between TFCI and these components.

The measured total heat exchanged in the system Q is assessed using the TFCI helium enthalpy difference between inlet and outlet. The analysis shows that the characteristic parameter p*h ($Q=p*h*\Delta T$, where p is the exchange perimeter, h is the heat transfer coefficient and ΔT is the temperature difference between TFCI and mandrel/joints) is in the order of < 1 W/K for the mandrel (calculated at the beginning of the run) and in the range 7-10 W/K for each joints. The p*h values for the joints is an approximated average in the central part of the run, i.e. after the initial transient and before Joule heat generation at the end (Table A1 and Fig. A3).

In the simulations the contribution of the mandrel heat exchange is set to zero since the p*h is negligible compared to the p*h of the joints. This assumption considerably simplifies the simulation model since it eliminates the choice of the reference mandrel temperature, which is anyway not available in the experimental data. In fact, the mandrel is sensitive to the 'history' of the experiment before the start of the run while data are only available for t >=0s. For example, in several of the investigated runs the coolant temperature at the outlet of the mandrel cooling pipe (which is representative of the mandrel temperature) is above the TCFI conductor temperature, i.e.the mandrel is warming up the TFCI rather than cooling it. This heat load on the mandrel is likely due to eddy currents losses generated by charging of the background CSMC at t < 0s.

Heat generation in both joints is accounted for by using a constant electrical resistance R_{joint}, obtained from the experimental results of current and voltage in the bottom joint (Table A1). We use the signal ITF_VD_JB because the signal at the top joint appears to be unreliable. The average value of all investigated runs is $R_{joint} = 2$ nΩ. The approximation of using an average value is justified by the fact that in both joints the heat generation is considerably smaller than the cooling.

Run #	t_{end} (s)	V_BOT (V)	I_{TFCI} (kA)	R (Ohm)	Qj_{jnt} (W)	ph_{jnt} (W/K)
Note ->		(a)		(b)	(c)	(d)
40-3	5267	71.0E-6	31.775	2.23E-9	2.019	7.0
43-3	4567	56.0E-6	17.609	3.18E-9	0.6202	8.0
44-2	6199	82.0E-6	46.030	1.78E-9	4.238	7.0
52-3	3581	74.0E-6	34.329	2.16E-9	2.357	7.0
57-3	4284	84.0E-6	46.060	1.82E-9	4.243	7.5
63-2	7532	58.0E-6	17.682	3.28E-9	0.6253	8.0
68-2	4453	60.0E-6	17.685	3.39E-9	0.6255	8.0
85-3	5744	84.0E-6	46.085	1.82E-9	4.248	9.0

(a) upper joint signal (lower joint signal V_BOB not reliable)
(b) Joint resistance, $R=V\_BOT/I_{TFCI}$
(c) total using the average $R = 2.0 \times 10^{-9}$ Ω
(d) average value in the final part of the run, before heat generation starts

Table A1. Heat exchange at joints

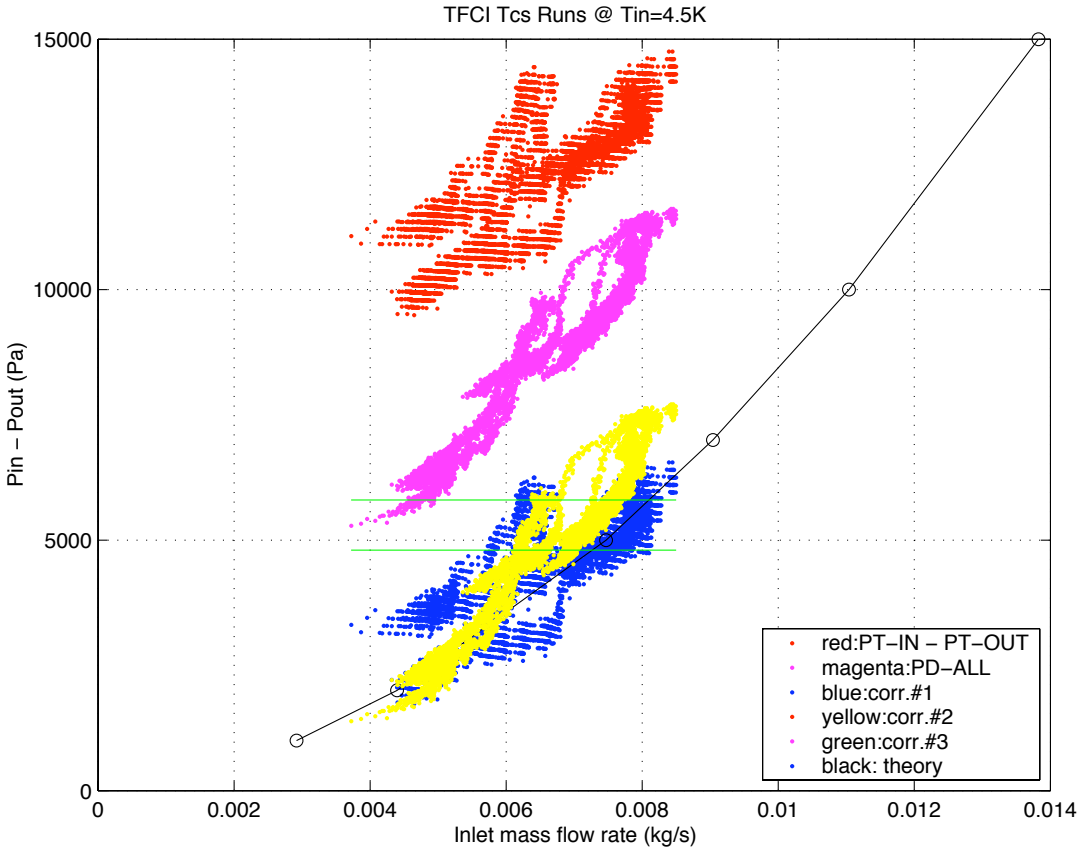

Figure A1. Pressure drop as a function of inlet mass flow rate for 7 T_{cs} runs. The initial temperature is ~4.5 K. The red cloud of data is the difference between the raw signals ITF_PT_IN - ITF_PT_OUT. The magenta cloud is the measured pressure drop (signal ITF_PD_ALL). The blue cloud is the red cloud with C3 = 7500 Pa (correction #1). The yellow cloud is the magenta cloud with C3 = 3900 Pa (correction #2). The range of the correction #3 is shown by the green lines. The black parabola is the theoretical curve obtained by running the THEA™ model at T=4.5K constant and using the following friction factors: (a) Katheder correlation without correction factor for the bundle, and (b) SHOWA correlation for the spiral (central channel).

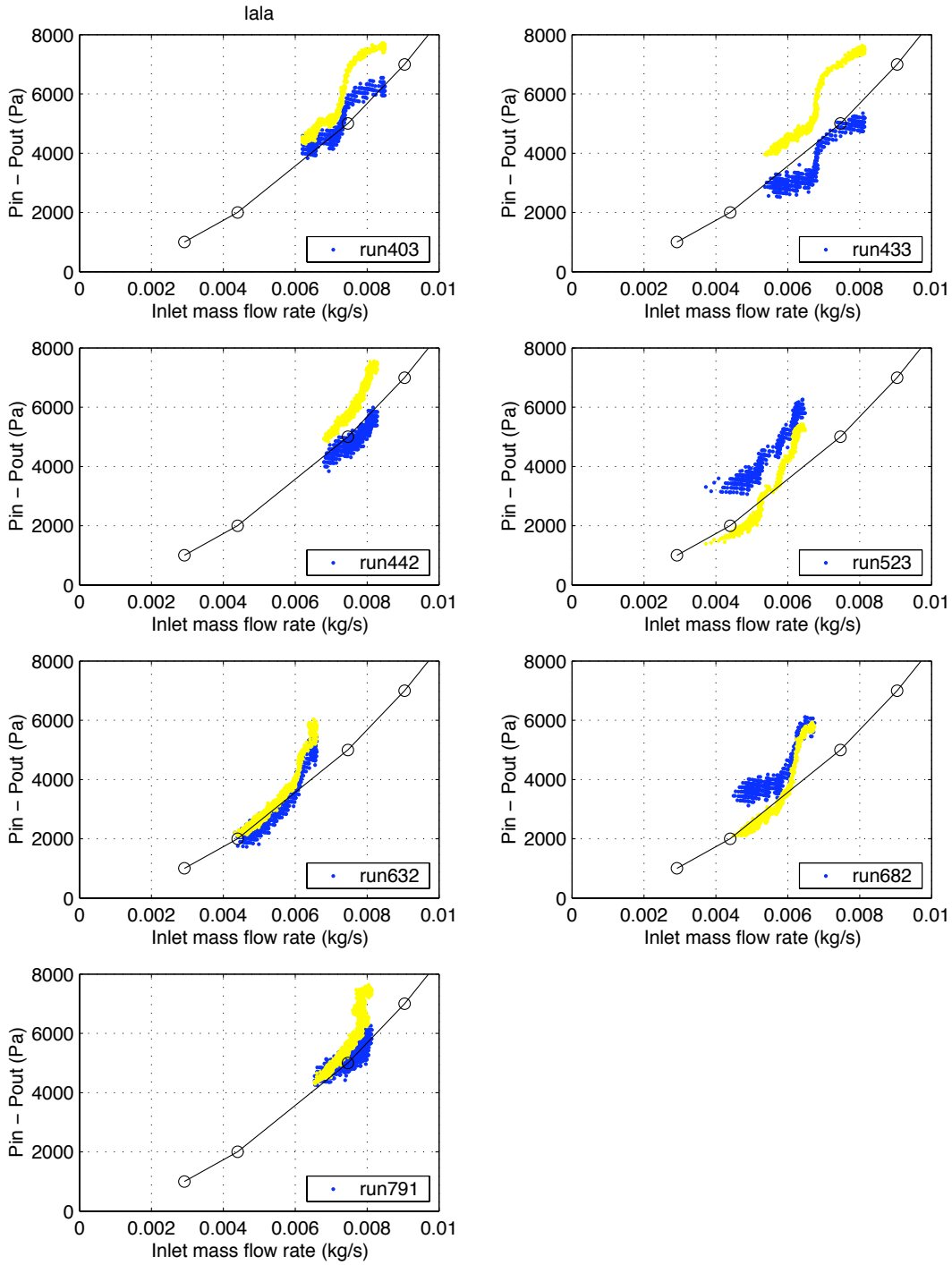

Figure A2. Details of pressure drop as a function of inlet mass flow rate for 7 T_{cs} runs. The meaning of the blue and yellow clouds as well as of the black parabola is explained in the caption of Figure A1.

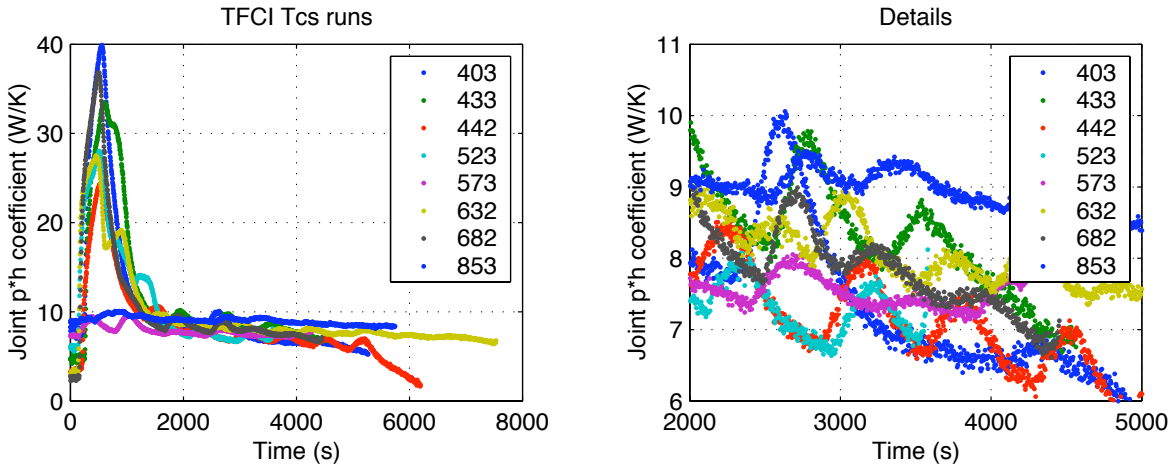

Figure A3. Heat exchange between TFCI conductor and joints (bottom/top), assuming a negligible contribution of the mandrel. The results are presented as the factor p*h as a function of time.

Appendix B. THEA™ Model

The total length of the thermal hydraulic model is 49.3 m: this includes the part of the winding embedded in the mandrel (38.7 m), the lower/upper 'tails', i.e. the conductor lengths connecting the windings to the joints (2x1.8 m), the lower/upper joints (2x0.5 m), and finally the lower/upper pipes leading to the terminations (2x3.0 m).

In the model the super strands are thermally coupled through a small thermal resistance and are cooled by helium flow through heat transfer at the wetted perimeter. Standard correlation (Dittus-Boelter) have been used for the calculation of the heat transfer coefficient. The factor 5/6 is used to calculate the wetted perimeter in the bundle.

The friction factor of the annulus is obtained using the Katheder correlation adjusted for the appropriate void fraction (37.9% in the TFCI conductor bundle, 22.0% in the joints) and without any correction factor. The latter choice is motivated by the very limited sensitivity of the overall results to a variation of this parameter in the range 1 - 3 (the ITER CICC value is ~2). The central channel is modeled using the CEA correlation for the SHOWA spiral, i.e. $4*f_{cc}=0.0756/Re^2$ [8] (we use the US notation for friction factor).

The super strands are electrically coupled through mutual inductances and intestrand conduction. These are calculated with the CryoSoft code 'Cable Interactive Designer' CID™ [12] (Fig. C1), using the average inter-petal contact resistance of the ITER CS1.1 and CS2 conductors after transverse cyclic loading (38 cycles, 650 kN/m), i.e. 4.2 and 2.1 μΩm, respectively. Conductance and inductance matrices generated by CID™ (in graphical form in Fig. C2 and C3) are then fed to THEA™.

Inputs to the THEA™ model are listed in Table C1 and C2, the post processing variables in Table C3.

Parameter	Unit	Pipe	Joint	Tail Winding Tail	Value
X range / lower part X range / middle part X range / upper part	m m m	0.0 - 3.0 46.3 - 49.3	3.0 - 3.5 45.8 - 46.3	3.5 - 5.3 5.3 - 44.0 44.0 - 45.8	
He cross section of bundle	m^2	AHB*0.01	AHB*0.423	AHB	AHB=3.9984E-4
He cross section of hole	m^2	AHH	AHH	AHH	AHH=8.3323E-5
Hydraulic diameter of bundle	m	DHB*0.01	DHB*0.423	DHB	DHB=4.7917E-4
Hydraulic diameter of hole	m	DHH	DHH	DHH	DHH=10.300E-3
Model for bundle - void fraction	 %	Smooth	Katheder 22.0	Katheder 37.9 (l)	
Model for hole		Smooth	Showa	Showa	
Perforation hole-bundle	-	1.0	PER	PER	PER=2.7750E-1
Wetted perimeter hole-bundle	m	1.0	WP	WP	WP=3.5500E-2 (c)
Wetted perimeter (T-Bundle)	m	0.0	WP*0.5	WP	WP = (e)
Wetted perimeter (T-Hole)	m	3.2358E-2 (b)	WP	WP	WP = (f)
Cross section of Insulation	m^2	1.0E-8	CS	CS	CS=3.5500E-4
Cross section of Ti jacket	m^2	5.9862E-5	CS*10.0	CS	CS=2.5573E-4
Cross section of Ti spiral	m^2	1.0E-8	CS	CS	CS=6.0363E-5
Cross section of Petals - Copper - Nb3Sn	 m^2 m^2	 CS*0.01 CS*0.01	 CS CS	 CS CS	 CS=3.7766E-4 (h) CS=2.4524E-4 (i)

(b) pipe perimeter
(c) spiral half perimeter = PHTHB
(e) WP: petal=2.5634 (g), spiral=3.5500E-2 (c), Ti jacket=9.0396E-2 (=PHTJ), insulation=0.0
(f) WP: petal=0.0, spiral=3.5500E-2 (c), Ti jacket=0.0, insulation=0.0
(g) =PHTC, 1/6=4.2723E-1
(h) 1/6=6.2944E-5
(i) 1/6=4.0873E-5
(l) Chen-Yu (St. Petersburg 2002): 37.9% with corners, 34.3% without corners

Table B1. Thermal hydraulic input parameters

Run #	I_{TFCI} (kA)	I_{CSMC} (kA)	n-value (-)	Qj_{jnt} (W)	ph_{jnt} (W/K)	t_{end} (s)
40-3	31.775	40.140	7.1 - 8.6	2.019	7.0	5267
43-3	17.609	40.842	6.1 - 7.6	0.6202	8.0	4567
44-2	46.030	41.663	7.6 - 9.3	4.238	7.0	6199
52-3	34.329	34.927	9.4 - 10.2	2.357	7.0	3581
57-3	46.060	16.077	10.4 - 11.7	4.243	7.5	4284
63-2	17.682	40.814	5.7 - 6.7	0.6253	8.0	7532
68-2	17.685	40.832	5.6 - 6.4	0.6255	8.0	4453
85-3	46.085	16.070	9.0 - 11.8	4.248	9.0	5744

Table B2. Operational input parameters

THEA™ support	THEA™ target	THEA™ coordinate X (m)
Hydraulic H2 (hole)	Helium pressure @ inlet	0.0
	Helium pressure @ outlet	49.3
	Helium temperature @ inlet	0.0
	Helium temperature @ outlet	49.3
	Helium mass flow rate @ inlet	0.0
	Helium mass flow rate @ outlet	49.3
Electric E1-E6	Resistive voltage 0203 (a)	37.695 (VT_03)/42.210 (VT_02)
	Resistive voltage 0304	33.180 (VT_04)/37.695 (VT_03)
	Resistive voltage 0405	28.665 (VT_05)/33.180 (VT_04)
	Resistive voltage 0506	24.150 (VT_06)/28.665 (VT_05)
	Resistive voltage 0607	19.635 (VT_07)/24.150 (VT_06)
	Resistive voltage 0708	15.120 (VT_08)/19.635 (VT_07)
	Resistive voltage 0809	10.605 (VT_09)/15.120 (VT_08)
	Resistive voltage 0910	6.090 (VT_10)/10.605 (VT_09)
Thermal T1-T6	Conductor temperature	= f(X)
	T_{cs}	= f(X)
	Current	= f(X)
	Magnetic field (b)	= f(X)
(a) The generic Resistive voltage AB is the difference between the average voltage at location X=B (i.e. the sum of voltages in the 6 at location B divided by 6) and the average voltage at location A (sum of voltages in the 6 super strands at location A divided by 6). The average turn length of TFCI = 4.515 m. (b) B_total = B_background + B_self		

Table B3. Post processing variables

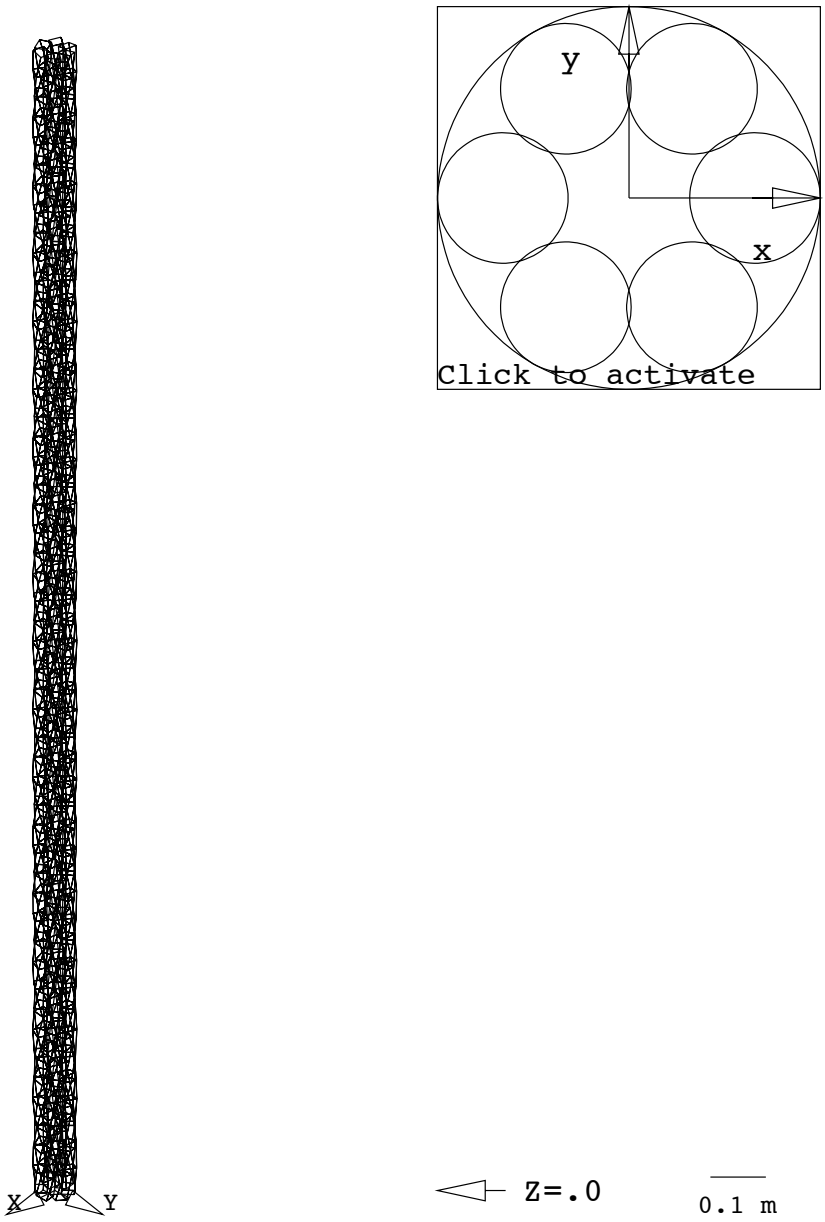

Figure B1. CID™ model of the 6 super strands.

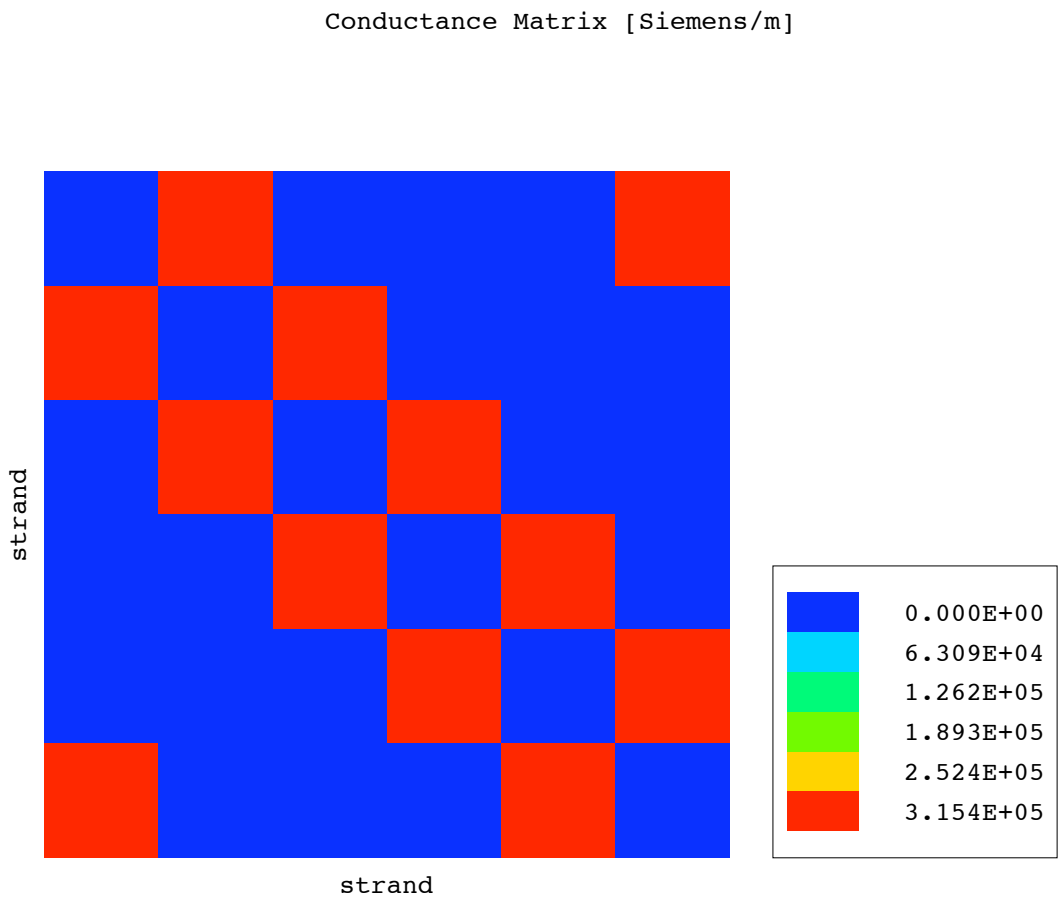

Figure B2. Conductance matrix (6 super strands) calculated by CID™.

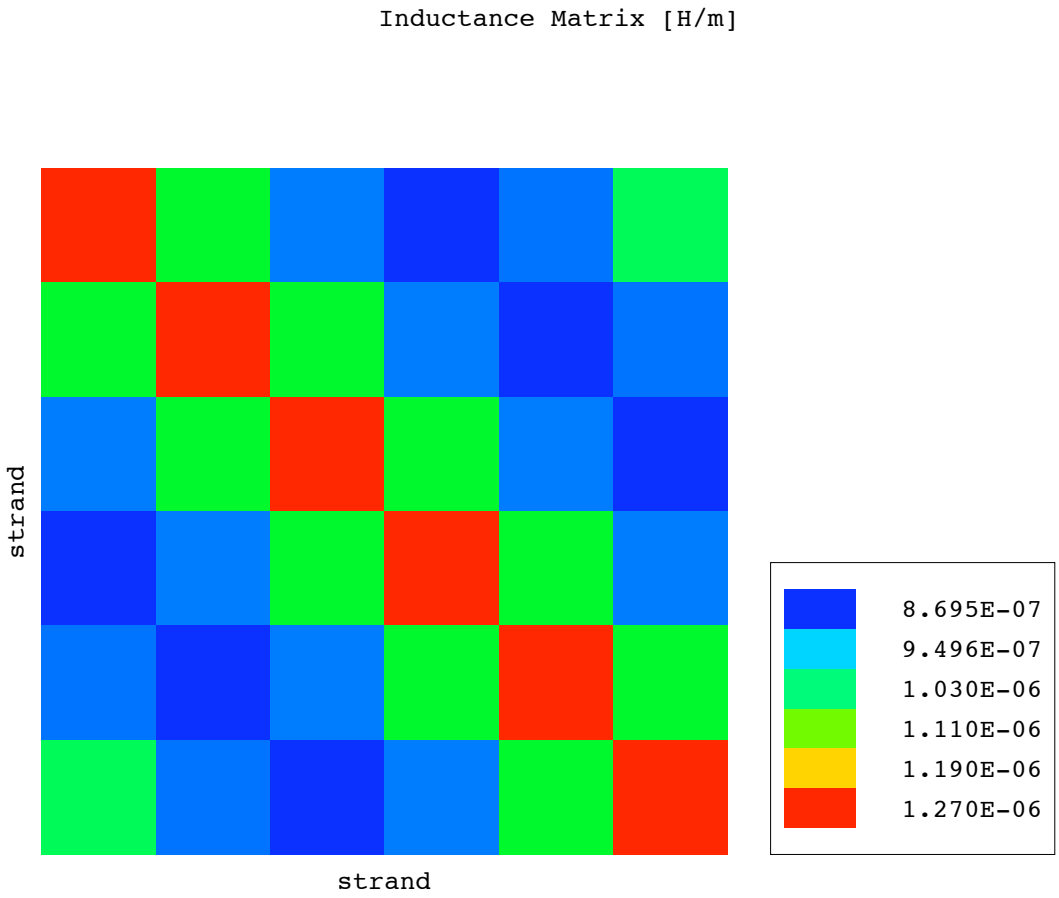

Figure B3. Inductance matrix (6 super strands) calculated by CID™.

Appendix C. Detailed results of run #44-2

We have selected the typical run #44-2 to present and discuss in detail of the results of the simulation, and to compare these results with the measurements. Run #44-2 is performed at high magnetic field, i.e. the peak field is 12.16 T, and high TFCI current (46 kA). The evolution ends at t_{end} = 6199 s.

The 'optimal' solution is found using the following values: n = 9.3 and ε = -0.5995%. The pressure correction factor is C3 = 5800 Pa.

C.1. Time histories

- Thermal hydraulic variables (see Fig. C1). It is only possible to directly compare simulations and measurements at inlet and outlet because of the lack of reliable sensors elsewhere. The simulated outlet temperature is in good agreement with the measured signal ITF_TC_OUT, i.e. the difference is in the order of less than few tenths of degree K. The simulated helium mass flow rates are underestimated with respect to the measured values, e.g. < 0.5 g/s at the inlet (ITF_FCT_INc) and < 0.2 g/s at the outlet (ITF_FCT_INc). The TFCI is operated in a range of 7-8 g/s and the relative error is < 10%. As discussed elsewhere in this report, although the choice of the pressure drop correction (i.e. outlet pressure as BC) has an influence on the dm/dt results, it has only a marginal influence on the other simulated results, as reported in more detail in Appendix F.
- Electrical variables (see Fig. C2). In general the simulated resistive voltage is underestimated near the inlet while the agreement with the measurements improves along the conductor length and becomes good near the outlet. This results is influenced by the strategy adopted for the simulations, namely that the assessment of the 'optimal' combination of n-value and ε is based on the minimization of the error on V0304 at take off. In particular, at take off time or at the end of current sharing the maximum difference between simulation and experiment is ~ 0.6 mVolt (V0809 @ X = 10.605/15.120 m) and the minimum difference is < 0.2 mVolt (V0304 @ X = 33.180/37.695 m). Outside current sharing, the agreement simulation/measurement is good for all voltage taps except V0809 (the signal ITF_VD_0203 has a very high noise and cannot be compared).

C.2. Distribution along the TFCI conductor length

We present here the simulated results along the nodal coordinate X as two snapshots, at t_{end} and shortly afterwards. These results provide a virtual instrument for the interpretation of the experiment since there are no reliable DAS signals along the conductor length (except the voltage taps measurements).

- Snapshot at t = t_{end}. There is a parabolic increase of the temperature from lower to upper end of the winding (3.5 m < X < 45.8 m). Elsewhere, the drop of temperature is driven by the heat exchange in the lower/upper joints (Fig. C3). The temperature is not homogenous in the conductor cross section, i.e. the difference between the thermal components T5-T6 and the other components is ~ 0.15 K. The asymmetric temperature distribution in the conductor cross section is a simulation artefact occurring although the simulation model is fully symmetrical, e.g. ideal electrical joint properties, conductor cross section properties, etc. The

corresponding current sharing is limited to ~ 300 A. The peak temperature is ~ 8.05 K at X = 42.7 m in T5 (or in T6, slightly downward) and the current sharing temperature is ~ 7.9 T at the total magnetic field of ~ 11.8 T. (Fig. C4). At the peak magnetic field (~ 12.16 T), which is located near the mid point of the TFCI winding (X ~ 25 m), the conductor temperature in T5-T6 is ~ 7.46 K and T_{cs} = 7.7 K (Fig. C5).

- Snapshot at t = 6200 s (t_{end} + 1s). At this time the take off is fully developed and the conductor temperature has reached ~ 50 K at X = 42.5 m (Fig. C6 and C7). Current is shared between super strands T1-T2 (~ 12 kA each) and T5-T6 (~ 3 kA each), with super strand T3-T4 in equilibrium (~ 8 kA each).

C.3. Summary

The agreement between simulated and experimental signals during the complete run 442, and in particular during the most critical phase, i.e. current sharing phase and take off time, is within limits deemed acceptable for this study.

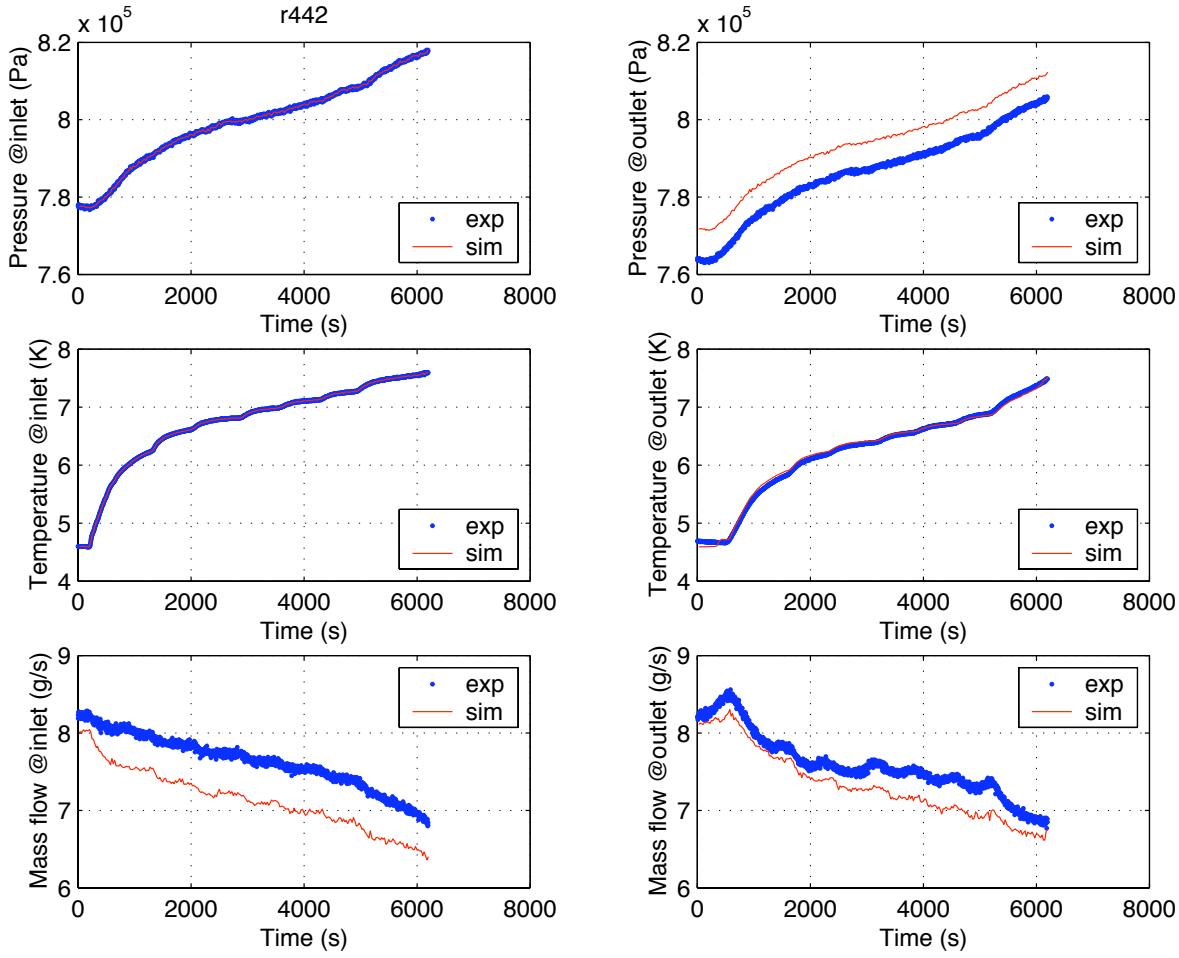

Figure C1. Results of run #44-2 with C3 = 5800 Pa, n = 9.3, ε = -0.5995%. Comparison between experimental (blue) and simulated (red) time history of thermal hydraulic variables.

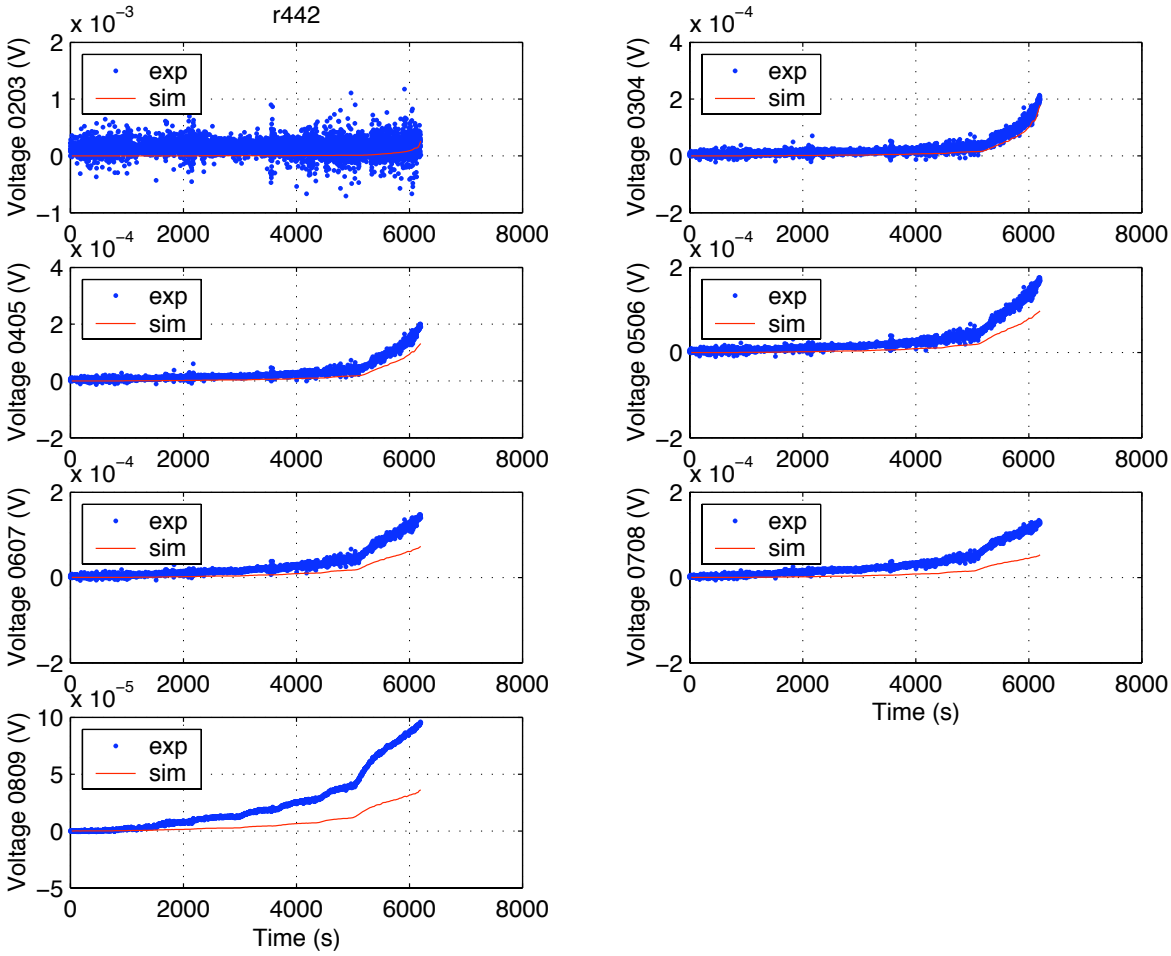

Figure C2. Results of run #44-2 with C3 = 5800 Pa, n = 9.3, ε = -0.5995%. Comparison between experimental (blue) and simulated (red) time history of resistive voltages.

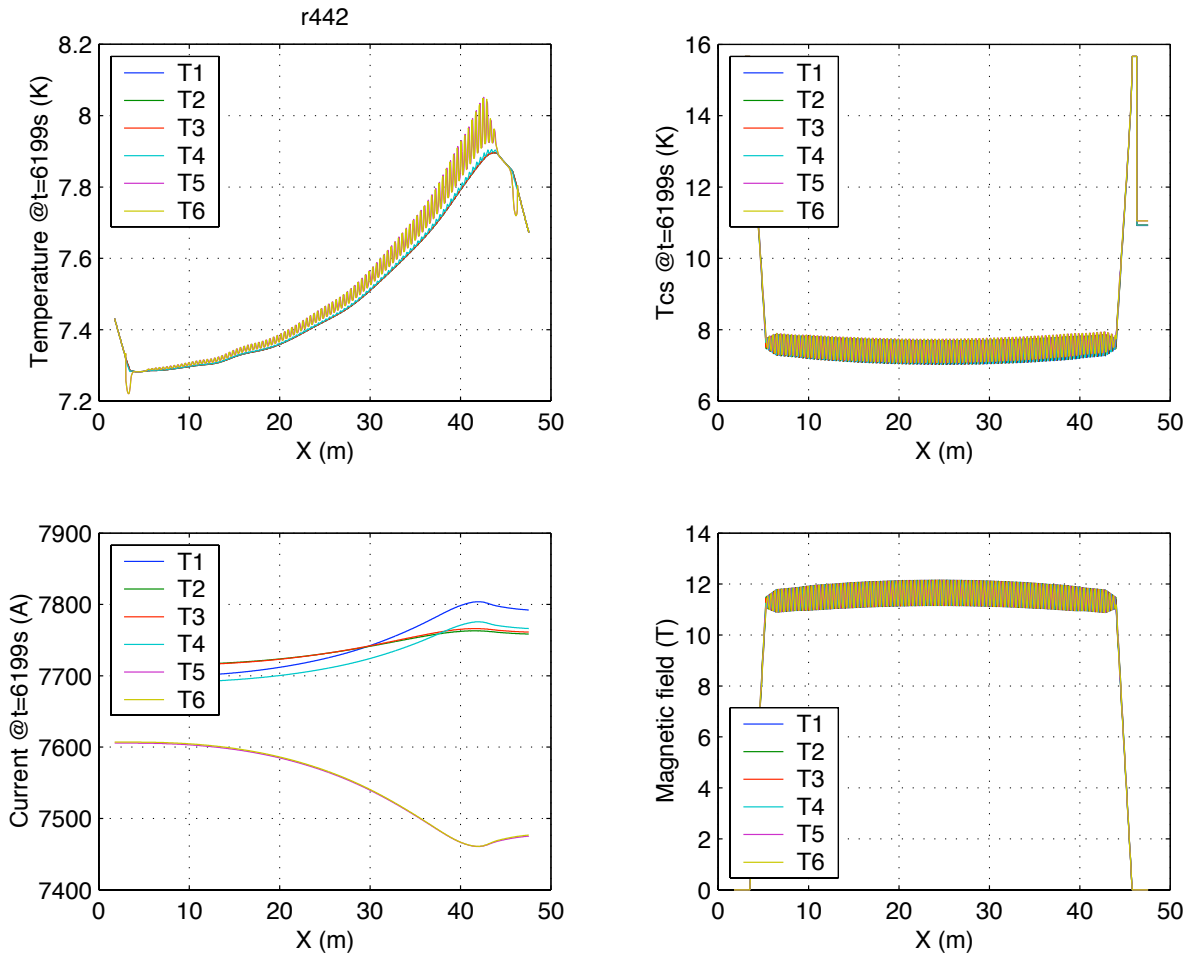

Figure C3. Results of run #44-2 with C3 = 5800 Pa, n = 9.3, ε = -0.5995%. Distribution of simulated temperature, T_{cs}, current and magnetic field in the 6 super strands along the complete conductor length, at the end of the run (t = 6199 s). Experimental data for these variables are not available. The asymmetric temperature distribution in the conductor cross section is a simulation artefact occurring although the simulation model is fully symmetrical, e.g. ideal electrical joint properties, conductor cross section properties, etc.

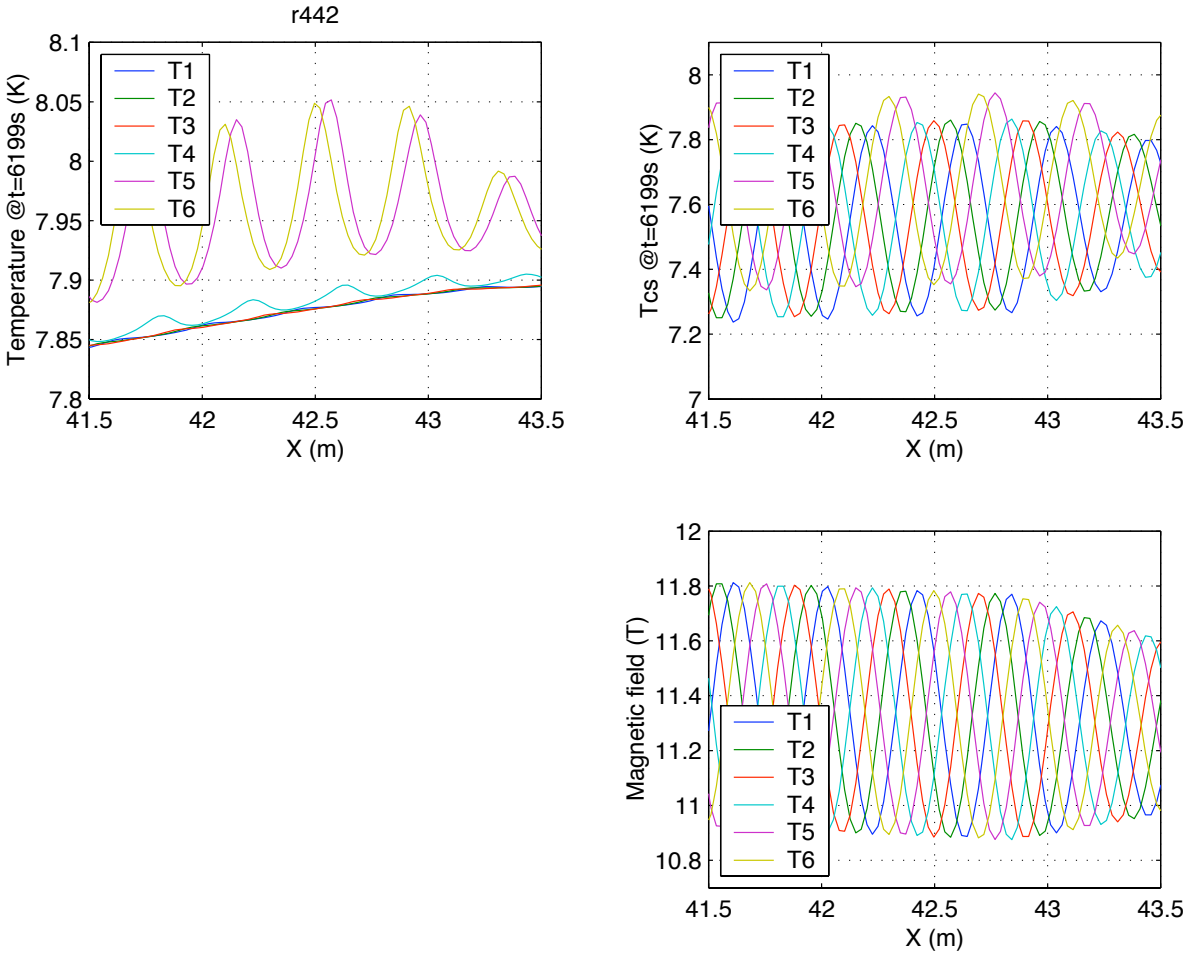

Figure C4. Results of run #44-2 with C3 = 5800 Pa, n = 9.3, ε = -0.5995%. Distribution of simulated temperature, T_{cs} and magnetic field in the 6 super strands along the a fraction of the conductor length (41.5m<X<43.5m), at the end of the run (t = 6199 s). Experimental data for these variables are not available. The asymmetric temperature distribution in the conductor cross section is a simulation artefact occurring although the simulation model is fully symmetrical, e.g. ideal electrical joint properties, conductor cross section properties, etc.

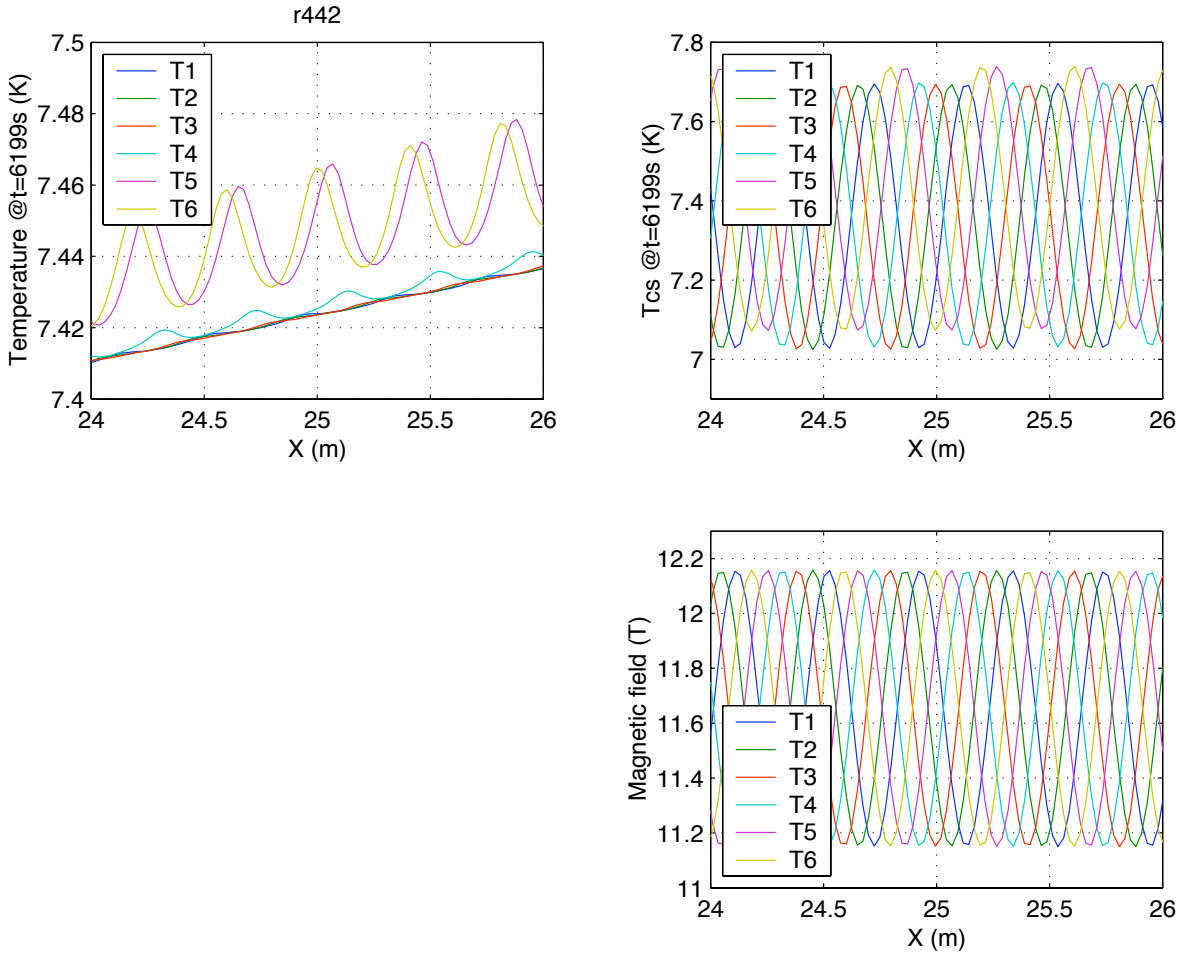

Figure C5. Results of run #44-2 with C3 = 5800 Pa, n = 9.3, ε = -0.5995%. Distribution of simulated temperature, T_{cs} and magnetic field in the 6 super strands along the a fraction of the conductor length (24.0m<X<26.0m), at the end of the run (t = 6199 s). Experimental data for these variables are not available. The asymmetric temperature distribution in the conductor cross section is a simulation artefact occurring although the simulation model is fully symmetrical, e.g. ideal electrical joint properties, conductor cross section properties, etc.

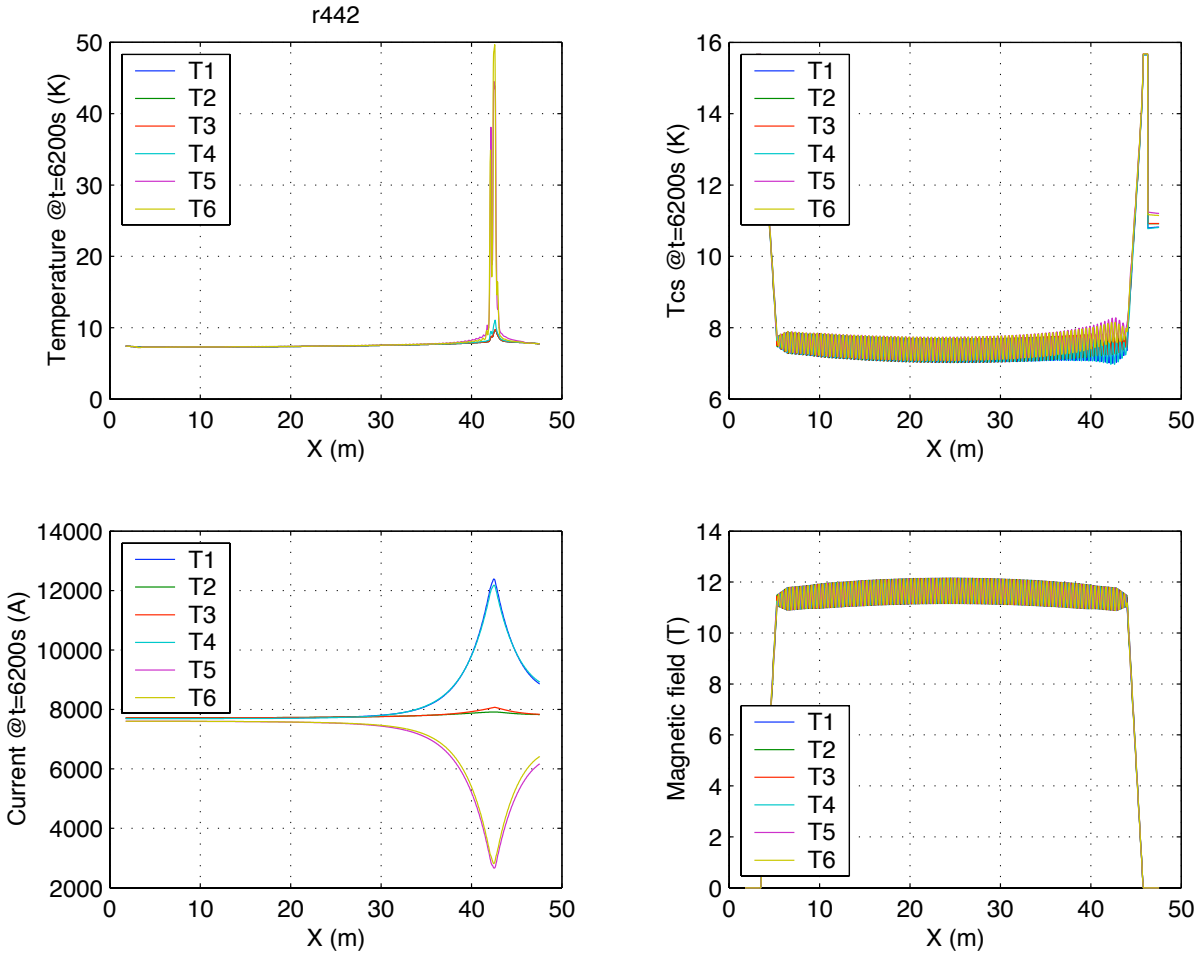

Figure C6. Results of run #44-2 with C3 = 5800 Pa, n = 9.3, ε = -0.5995%. Distribution of simulated temperature, T_{cs}, current and magnetic field in the 6 super strands along the complete conductor length, one second after the end of the run (t = 6200 s). Experimental data for these variables are not available. The asymmetric temperature distribution in the conductor cross section is a simulation artefact occurring although the simulation model is fully symmetrical, e.g. ideal electrical joint properties, conductor cross section properties, etc.

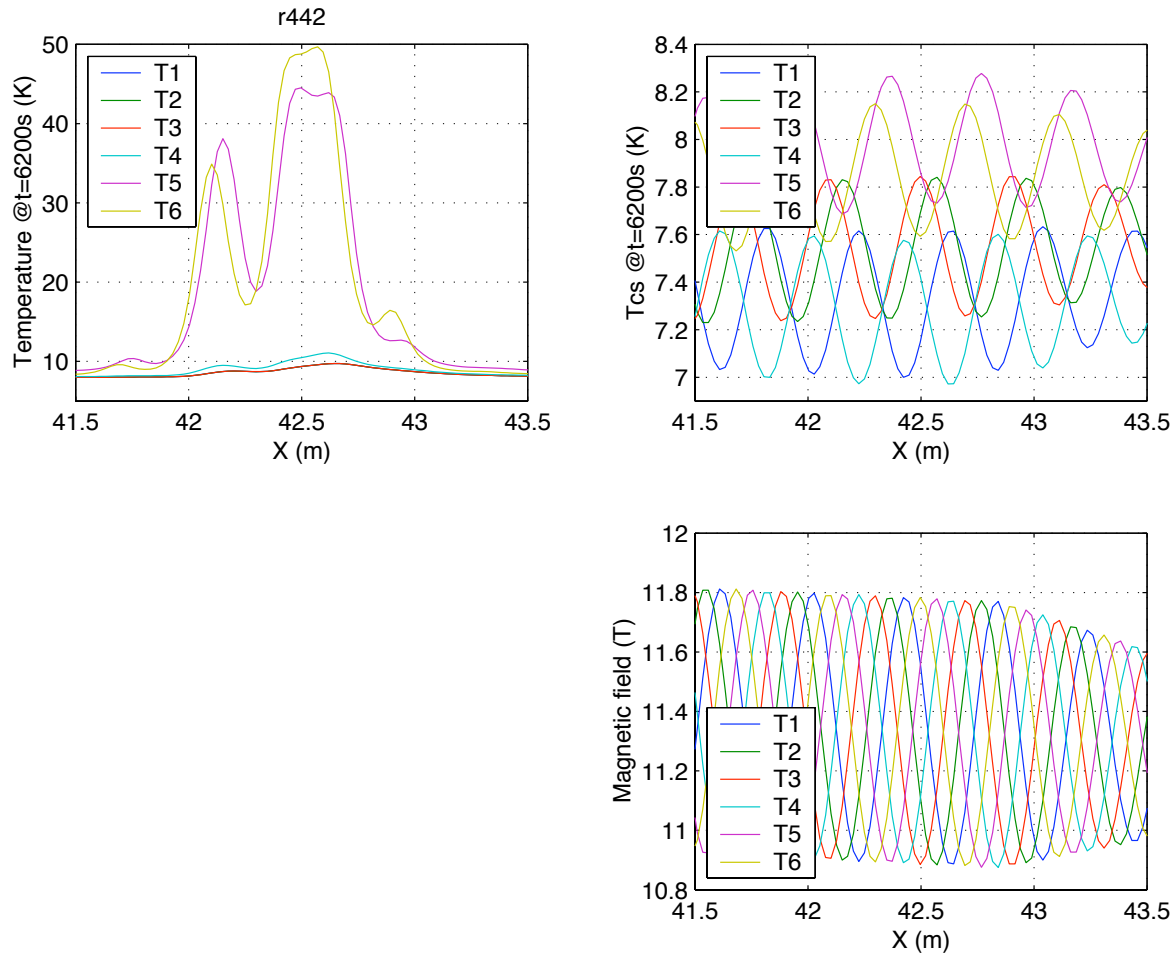

Figure C7. Results of run #44-2 with C3 = 5800 Pa, n = 9.3, ε = -0.5995%. Distribution of simulated temperature, T_{cs} and magnetic field in the 6 super strands along a fraction of the conductor length (41.5m<X<43.5m), one second after the end of the run (t = 6200 s). Experimental data for these variables are not available. The asymmetric temperature distribution in the conductor cross section is a simulation artefact occurring although the simulation model is fully symmetrical, e.g. ideal electrical joint properties, conductor cross section properties, etc.

This page is left intentionally blank.

Appendix D. Results of all runs

We present the results of the simulation of all T_{cs} runs, including two special cases (#57-3 and #85-3).

D.1. All runs except #57-3 and #85-3

The simulated results are qualitatively similar to those of run #44-2, described in detail in Appendix C. These results are presented in Fig. D1-D5 and in Table D1 (identical to Table 3).

- The selected pressure correction factor varies in the range 4800 Pa < C3 < 5800 Pa. At low values of C3 (run #52-3, #63-2, #68-2) the simulated outlet mass flow rate is overestimated with respect to the experimental one in the first 1/4 of the run and is closer to it in the following 3/4 of the run. At the upper value of C3 the reverse agreement for the outlet dm/dt applies (Appendix A).
- The 'optimal' n-value (n_{opt}) varies in the range between 7.6 (#43-3, #63-2 and #68-2) and 10.2 (#52-3), depending on the operating conditions. The n_{opt} is either equal or larger than the upper n values predicted by analysis of resistive voltage (Appendix G), i.e. there is a slightly lower degradation of the cable.
- The simulated 'optimal' fitting factor ε is independent of the electromagnetic load ($BI = B_{max} \times I_{TFCI}$). This is shown by the fact that in the range 202 kN/m < BI < 560 kN/m the fitting factor ε varies only between -0.5850% and 0.5995%. There is still no explanation for this surprising result, which is however in agreement with [10].
- The current sharing temperature T_{cs} varies between 7.04 K (#44-2) and 9.06 K (#43-3, #63-2 and #68-2). These results are obtained at $B = B_{max}$ using the TFCI strand data and the simulated ε. In general, these T_{cs} values are lower than those obtained from the experimental voltages (Appendix G).
- Simulated and measured resistive voltages are in excellent agreement at all voltage taps in run #52-3, #63-2 and #68-2, whereas the voltages of #40-3 have the same trend discussed for run #44-2, i.e. except at V0304 they are underestimated and the error increases in voltage taps located at decreasing values of the nodal coordinate X.

D.2. Run #57-3 and #85-3

Runs #57-3 and #85-3 are performed at low magnetic field (B_{max} ~ 5 T, at least a factor 2 lower than in other runs) and high helium temperature (~ 8 K at the beginning of the run). The simulation of these two runs is problematic because of

- premature quenches when using realistic n-values (even at ε = 0), or
- large (order of magnitude) underestimation of the resistive voltages when using unrealistically low n-values.

One possible explanation for this behavior is that the set of strand properties fed into the THEA model, which is based on measurements at high field (~ 11 T) and low temperature (~ 4.5 K), is not capable to give a realistic fit of cable properties at (considerably) different operating conditions. The optimization of the Summers parameters in the complete range of operating conditions of the Tcs runs is beyond the scope of this study.

Run #	B_{max} (T)	I_{TFCI} (kA)	BI (kN/m)	t_{end} (s)	C3 (Pa)	n (-)	ε (%)	T_{cs} (K)
Note								(c)
40-3	11.511	31.775	365.8	5267 (a)	5800	8.6	-0.5840	8.25 (8.46)
43-3	11.475	17.609	202.1	4567	5800	7.6	-0.5905	9.05 (n.a.)
44-2	12.158	46.030	559.6	6199	5800	9.3	-0.5995	7.04 (7.28)
52-3	10.124	34.329	347.5	3581	4800	10.2	-0.5850	8.95 (9.25)
57-3	5.147	46.060	237.1	4284	(b)	(b)	(b)	n.a. (11.72)
63-2	11.469	17.682	202.8	7532	5000	7.6	-0.5875	9.06 (n.a.)
68-2	11.474	17.685	202.9	4453	5300	7.6	-0.5891	9.05 (n.a.)
85-3	5.146	46.085	237.2	5745	(b)	(b)	(b)	n.a. (11.62)

(a) the simulation t = 0 s corresponds to the experimental t = 700 s.
(b) the simulation is not reliable with the given strand data because of either premature quench when using realistic n-values (even at ε = 0), or because of very large underestimation of the resistive voltages when using unrealistically low n-values
(c) at B=B_max. In parenthesis are the values obtained with the method described in Appendix G

Table D1. Operating conditions and summary of simulation results using the optimal combination of n-value and fitting parameter. Data ε and T_{cs} are computed results, other data are input parameters. For comparison, the corresponding n-values of the strand are in the range between 13 (at 17.6 kA) and 20 (at 20 kA).

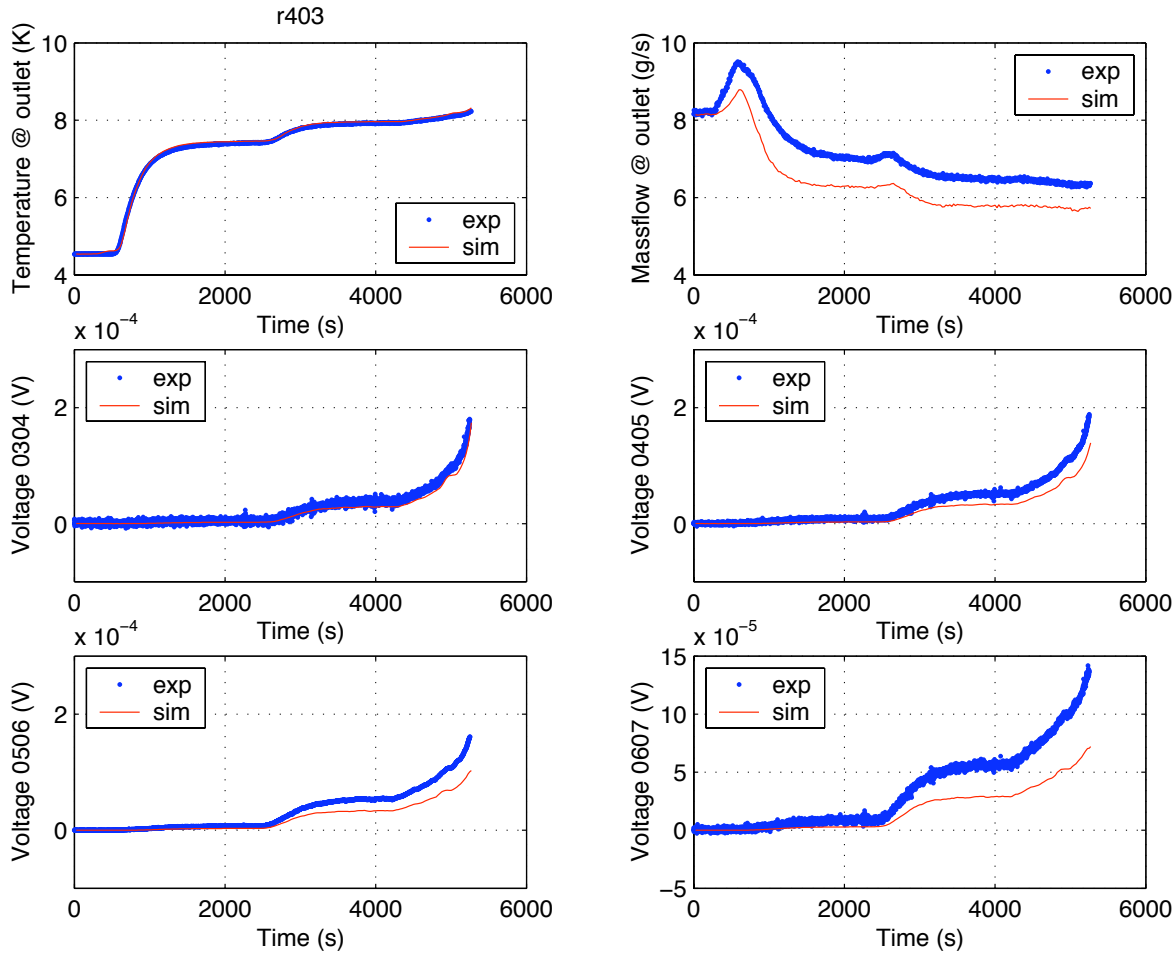

Figure D1. Results of run #40-3 with C3 = 5800 Pa, n = 8.6, ε = -0.5840%. Comparison between experimental (blue) and simulated (red) time history of thermal hydraulic variables.

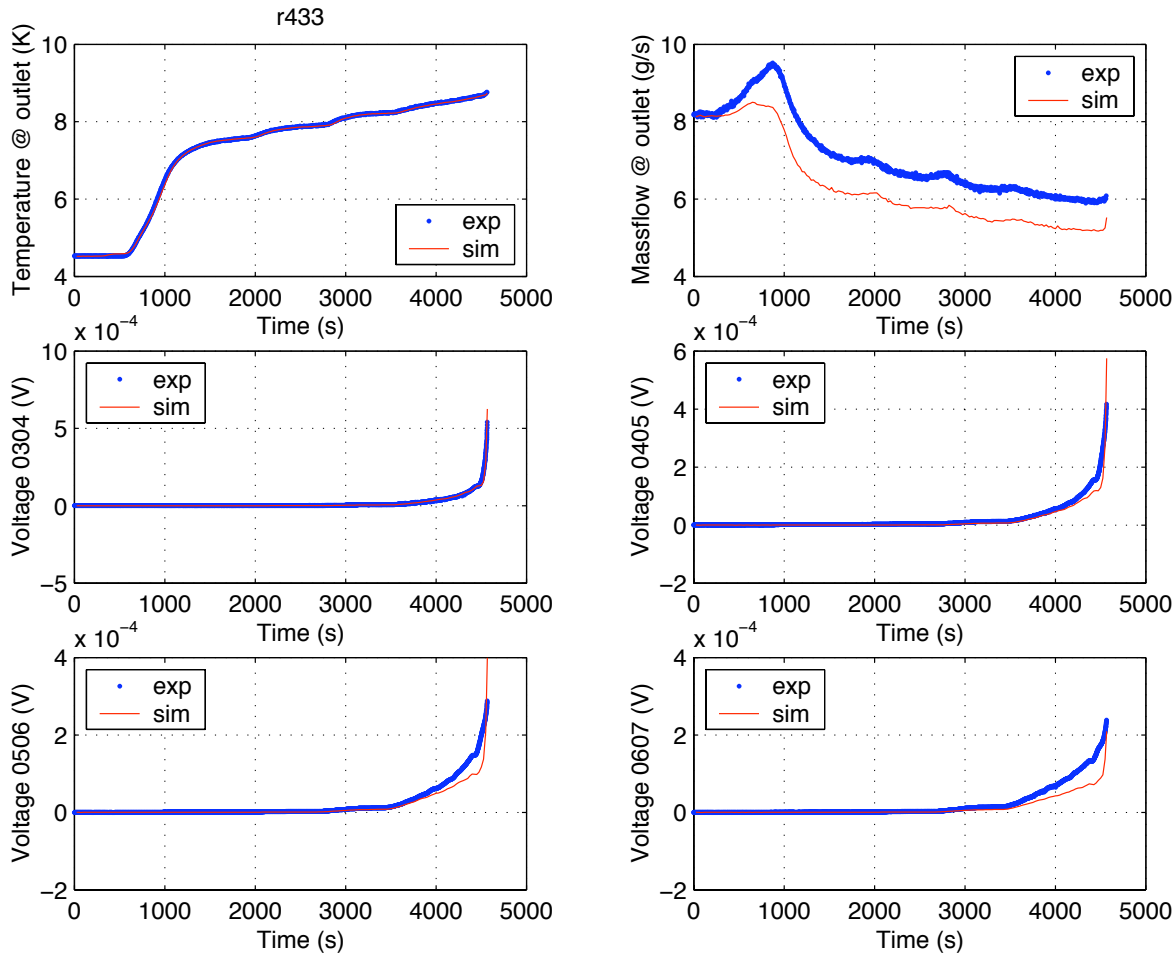

Figure D2. Results of run #43-3 with C3 = 5800 Pa, n = 7.6, ε = -0.5905%. Comparison between experimental (blue) and simulated (red) time history of thermal hydraulic variables.

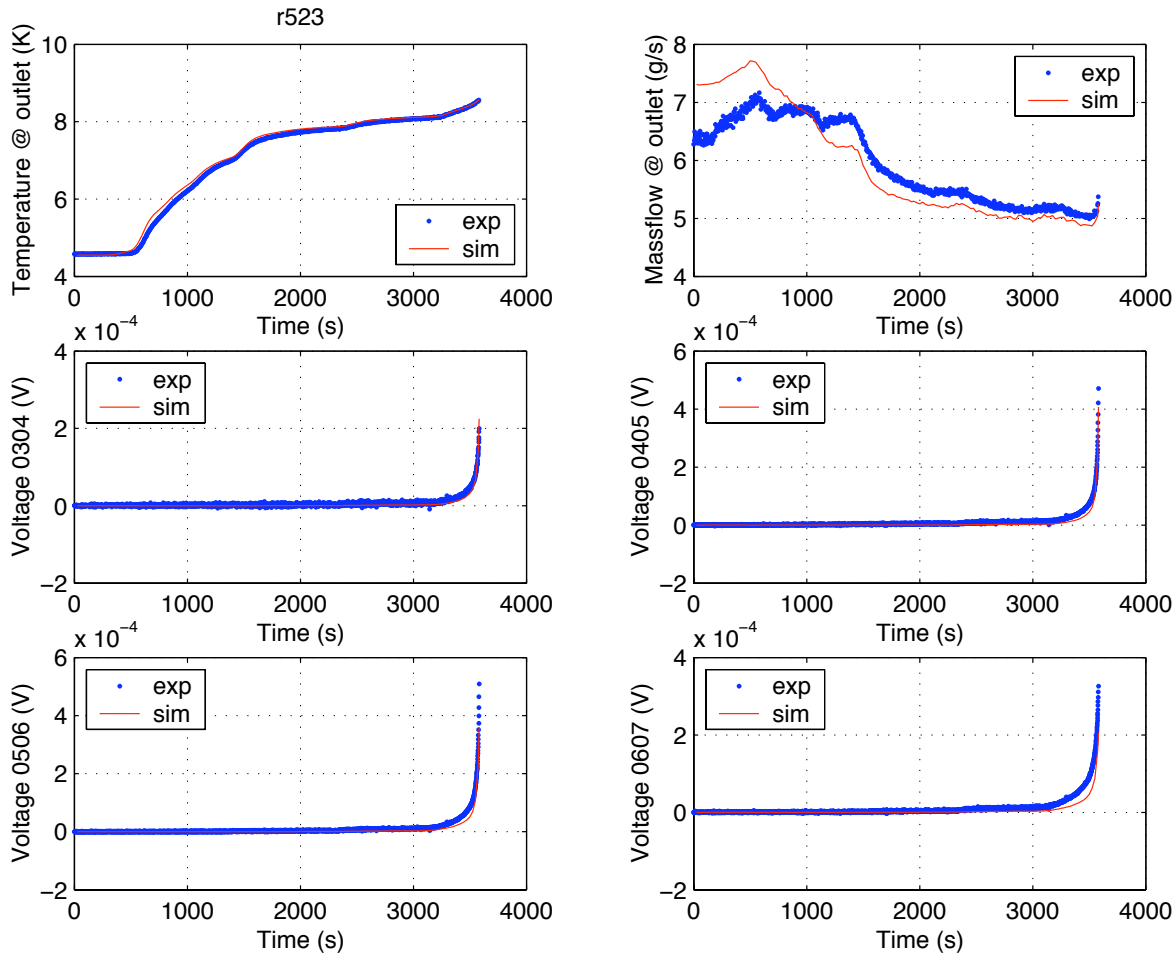

Figure D3. Results of run #52-3 with C3 = 4800 Pa, n = 10.2, ε = -0.5850%. Comparison between experimental (blue) and simulated (red) time history of thermal hydraulic variables.

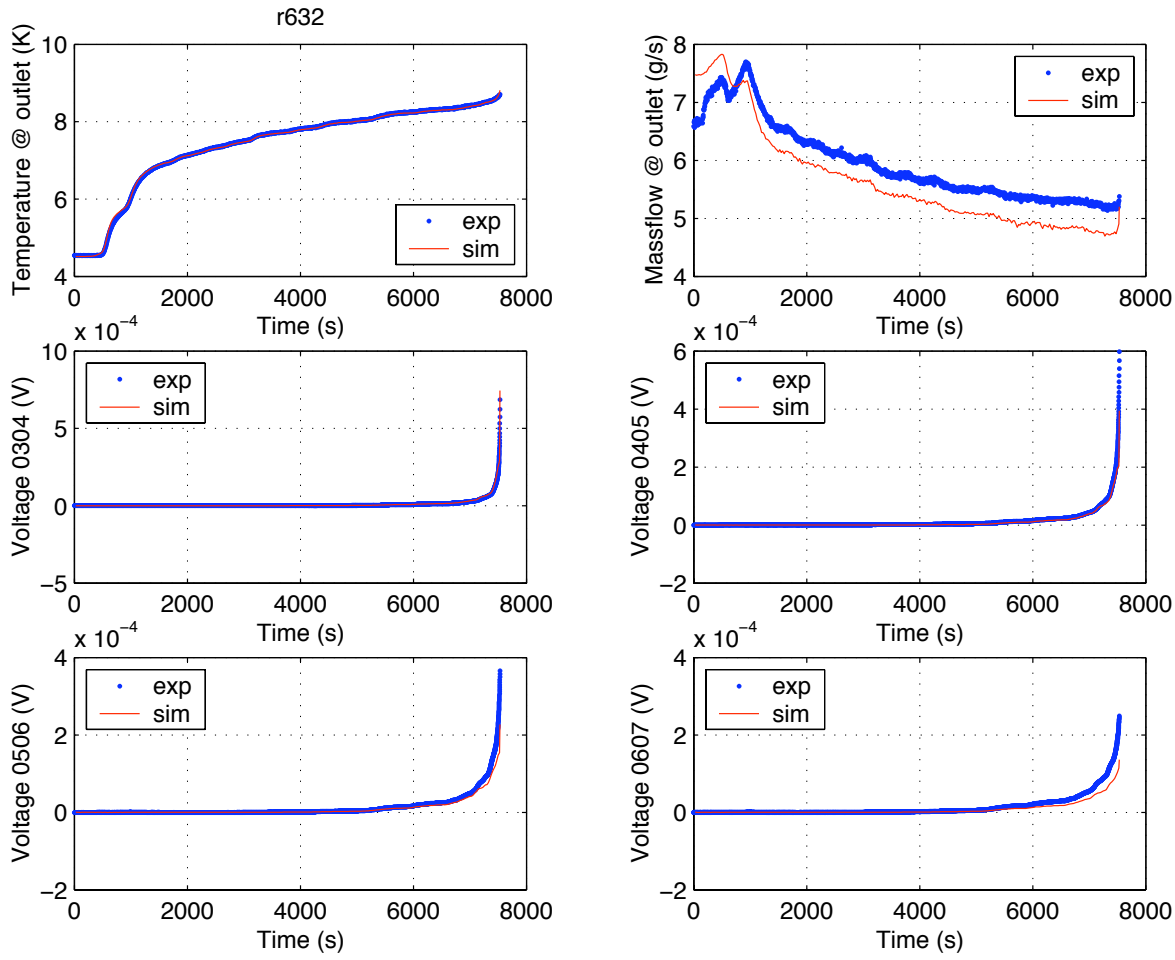

Figure D4. Results of run #63-2 with C3 = 5000 Pa, n = 7.6, ε = -0.5875%. Comparison between experimental (blue) and simulated (red) time history of thermal hydraulic variables.

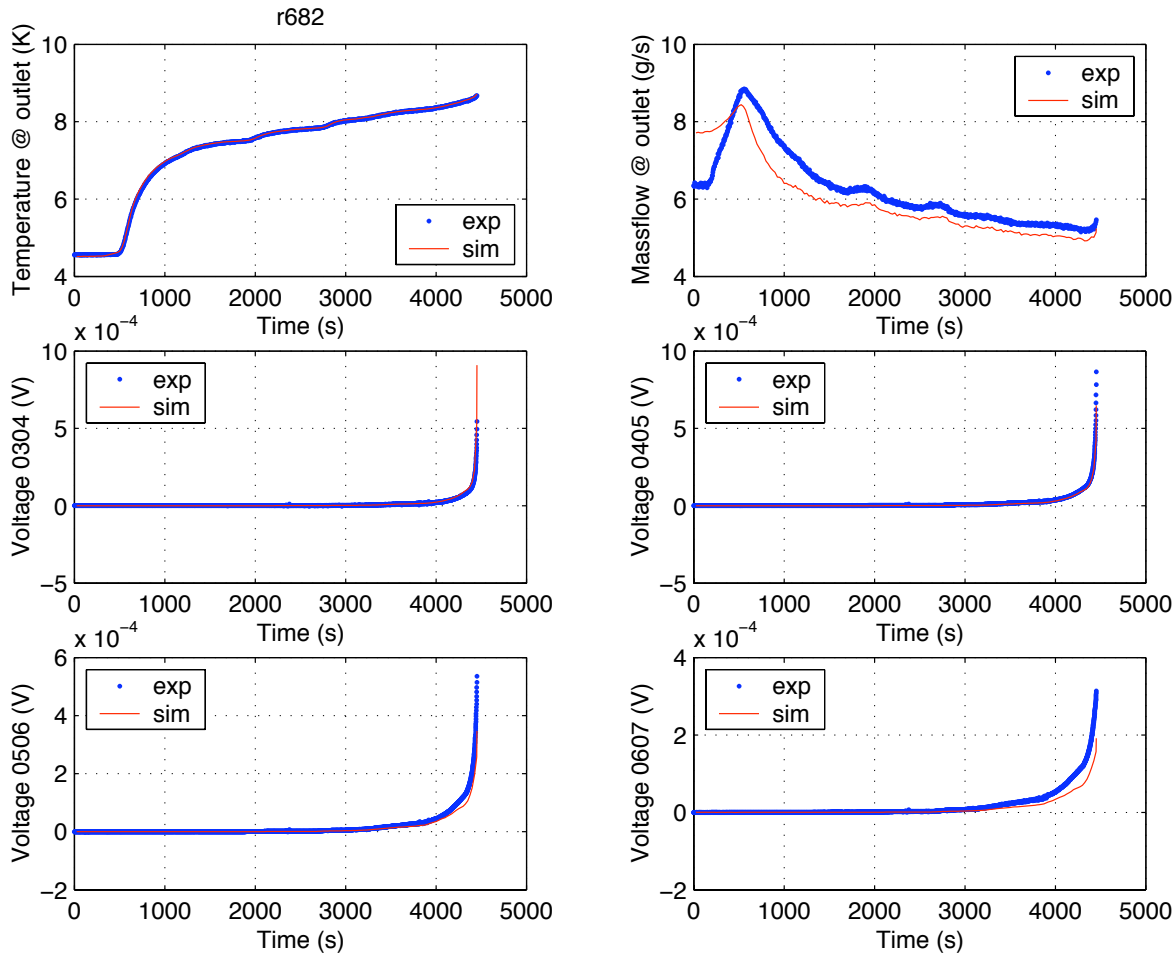

Figure D5. Results of run #68-2 with C3 = 5300 Pa, n = 7.6, ε = -0.5891%. Comparison between experimental (blue) and simulated (red) time history of thermal hydraulic variables.

This page is left intentionally blank.

Appendix E. Sensitivity to n-value

A limited sensitivity analysis is performed to assess the influence of the n-value on the relevant results of the simulation, e.g. total strain, outlet temperature, outlet mass flow rate, resistive voltage V0304 and current sharing temperature.

The study is applied to three runs at high magnetic field (> 11.4 T) and low, medium and high TFCI current, i.e. 17.6 kA (#43-4), 31.0 kA (#40-3) and 46.0 kA (#42.2). For each run we use the upper and lower n-values assessed through the experimental voltages (see Appendix G), as well as the value n = 7.6. In all runs the pressure correction factor is C3 = 5800 Pa.

E.1. Results

- The 'optimal' fitting parameter ε is selected after few iterations, e.g. larger negative values for lower n-values. Given that the way of selecting the 'optimal' parameters is quite approximate (see main text) and that the variation of n-value is small, in few cases the selected ε is the same for different n-values (Table E1).
- All output variables are quite insensitive to variation of the n-value. A summary at $t = t_{end}$ is shown in Fig. E1.
- In run #40-3 a decrease of the factor n produces a decrease of temperature at outlet and voltages whereas the mass flow rate is unchanged. The complete evolution is shown in Fig. E2, and details at current sharing in Fig. E3. In these figures the green curve (n = 7.6) lays behind the yellow curve (n = 7.1). Although n-values are different, ε is the same in both cases and this effect appears to dominate. At low TFCI current (run #43-3) all results are even more insensitive to changes of the n-value (Fig. E4 and E5). At high TFCI current (run #44-2) the results are qualitatively the same (with enhanced differences) as in run #40-3: it is possible to distinguish the results for all three n-values because different 'optimal' values of ε are selected.

Run #	B_{max} (T)	I_{TFCI} (kA)	BI (kN/m)	C3 (Pa)	n (-)	ε (%)	T_{cs} (K)
Note ->							(a)
40-3	11.511	31.775	365.8	5800	7.1	-0.5890	8.22
					7.6	-0.5890	8.22
					8.6	-0.5840	8.25
43-3	11.475	17.609	202.1	5800	6.1	-0.5965	9.02
					7.3	-0.5905	9.05
					7.6	-0.5905	9.05
44-2	12.158	46.030	559.6	5800	7.6	-0.6105	6.98
					8.4	-0.6045	7.01
					9.3	-0.5995	7.04
(a) $B=B_{max}$							

Table E1. Sensitivity of simulations to n-values

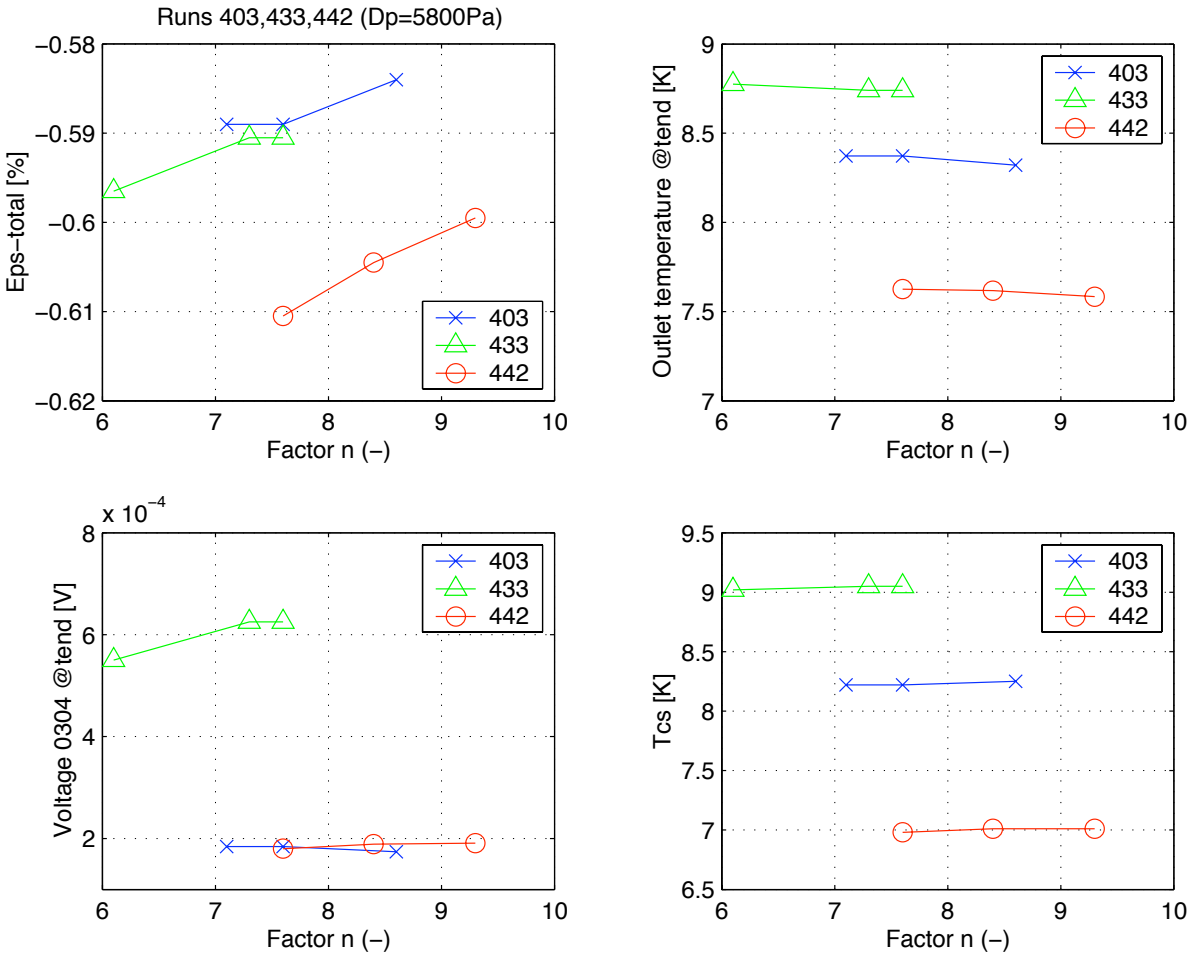

Figure E1. Sensitivity to n-value of the fitting parameter ε (Eps_total), T_{cs}, outer temperature and voltage V0304 at the end of run #40-3, #43-3 and #44-2. The pressure correction factor for all runs is C3 = 5800 Pa.

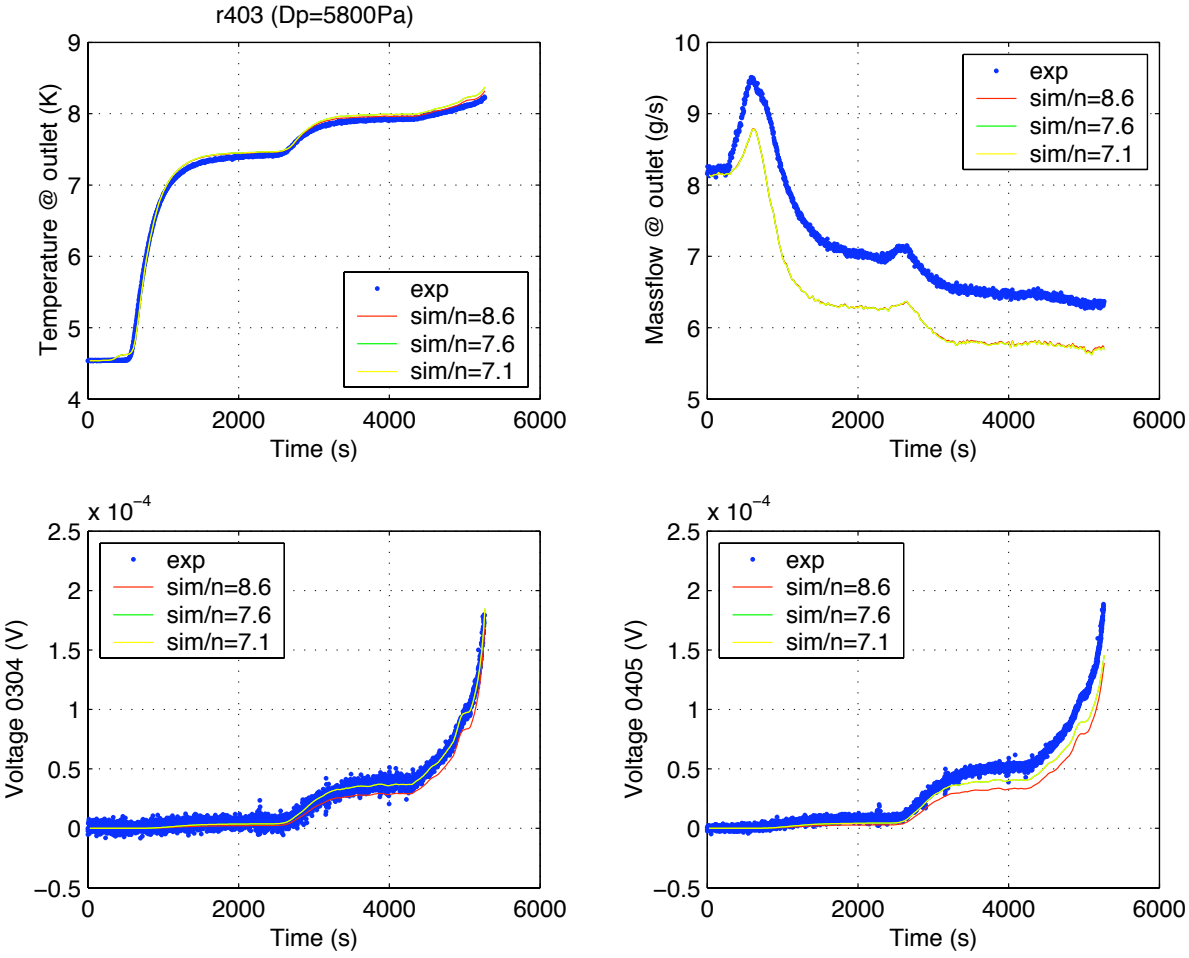

Figure E2. Sensitivity to n-value of run #40-3. Comparison between experimental (blue) and simulated (red: n = 8.6, green: n = 7.6 and yellow: n = 7.1) time history of thermal hydraulic variables and resistive voltages.

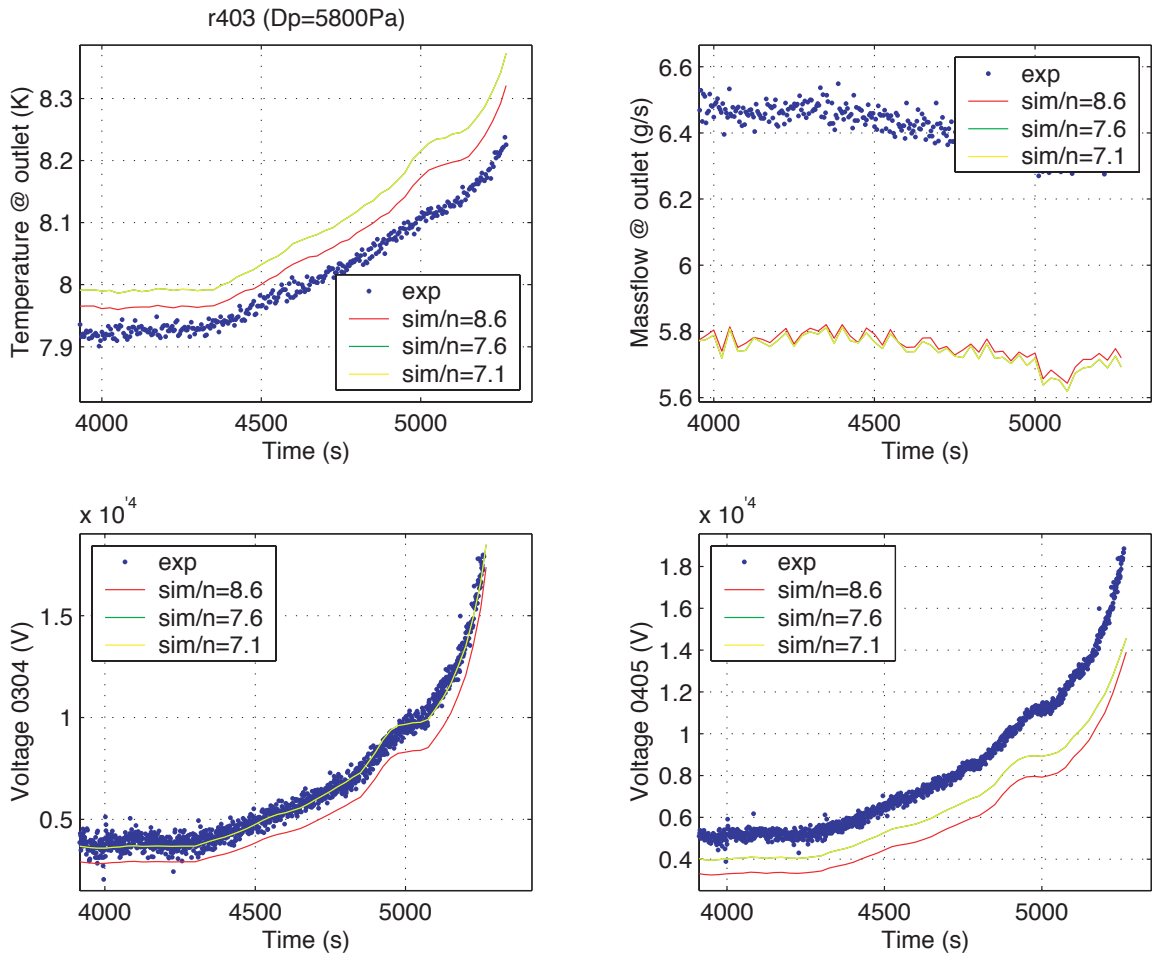

Figure E3. Sensitivity to n-value of run #40-3. Comparison between experimental (blue) and simulated (red: n = 8.6, green: n = 7.6 and yellow: n = 7.1) time history of thermal hydraulic variables and resistive voltages. Details in the final evolution of the run.

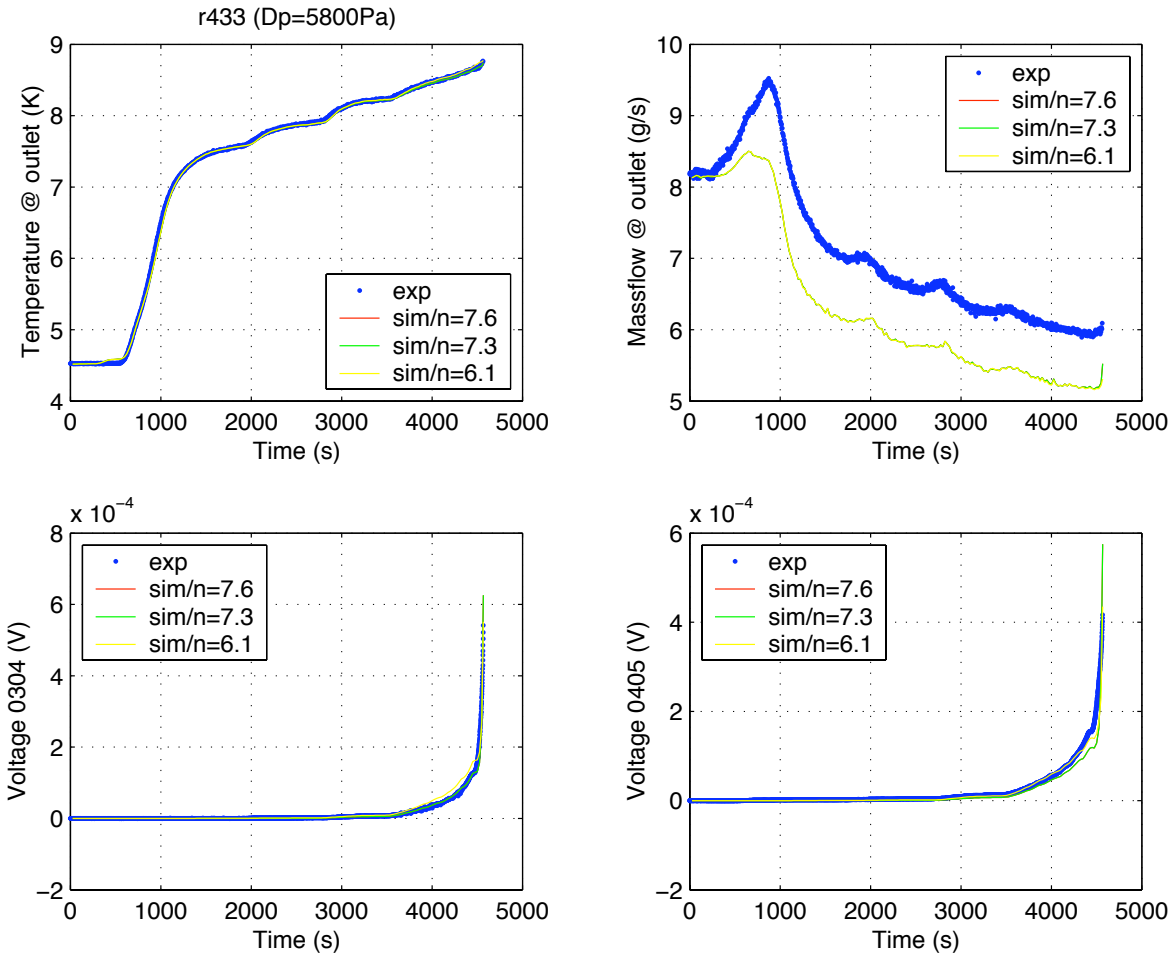

Figure E4. Sensitivity to n-value of run #43-3. Comparison between experimental (blue) and simulated (red: n = 8.6, green: n = 7.6 and yellow: n = 7.1) time history of thermal hydraulic variables and resistive voltages.

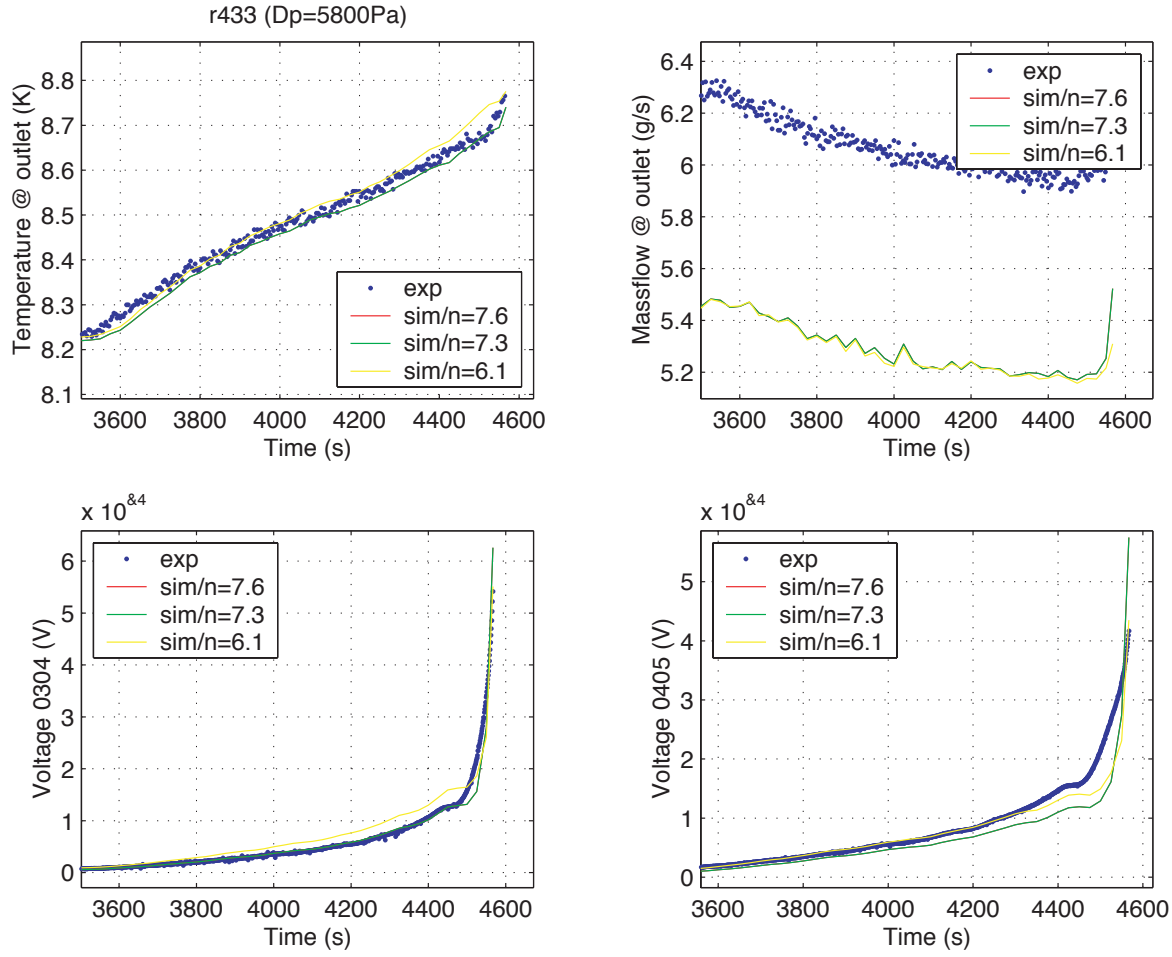

Figure E5. Sensitivity to n-value of run #43-3. Comparison between experimental (blue) and simulated (red: n = 8.6, green: n = 7.6 and yellow: n = 7.1) time history of thermal hydraulic variables and resistive voltages. Details in the final evolution of the run.

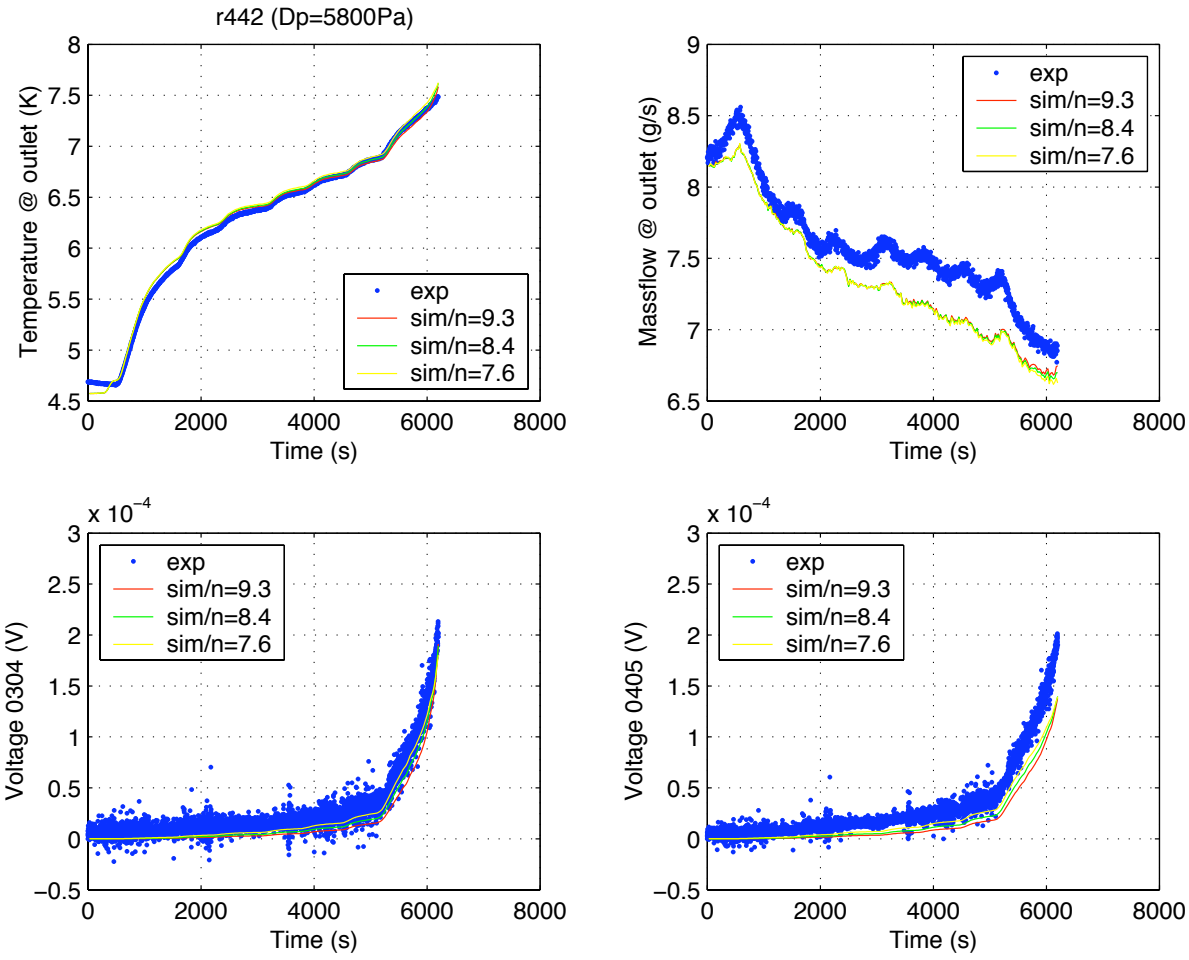

Figure E6. Sensitivity to n-value of run #44-2. Comparison between experimental (blue) and simulated (red: n = 8.6, green: n = 7.6 and yellow: n = 7.1) time history of thermal hydraulic variables and resistive voltages.

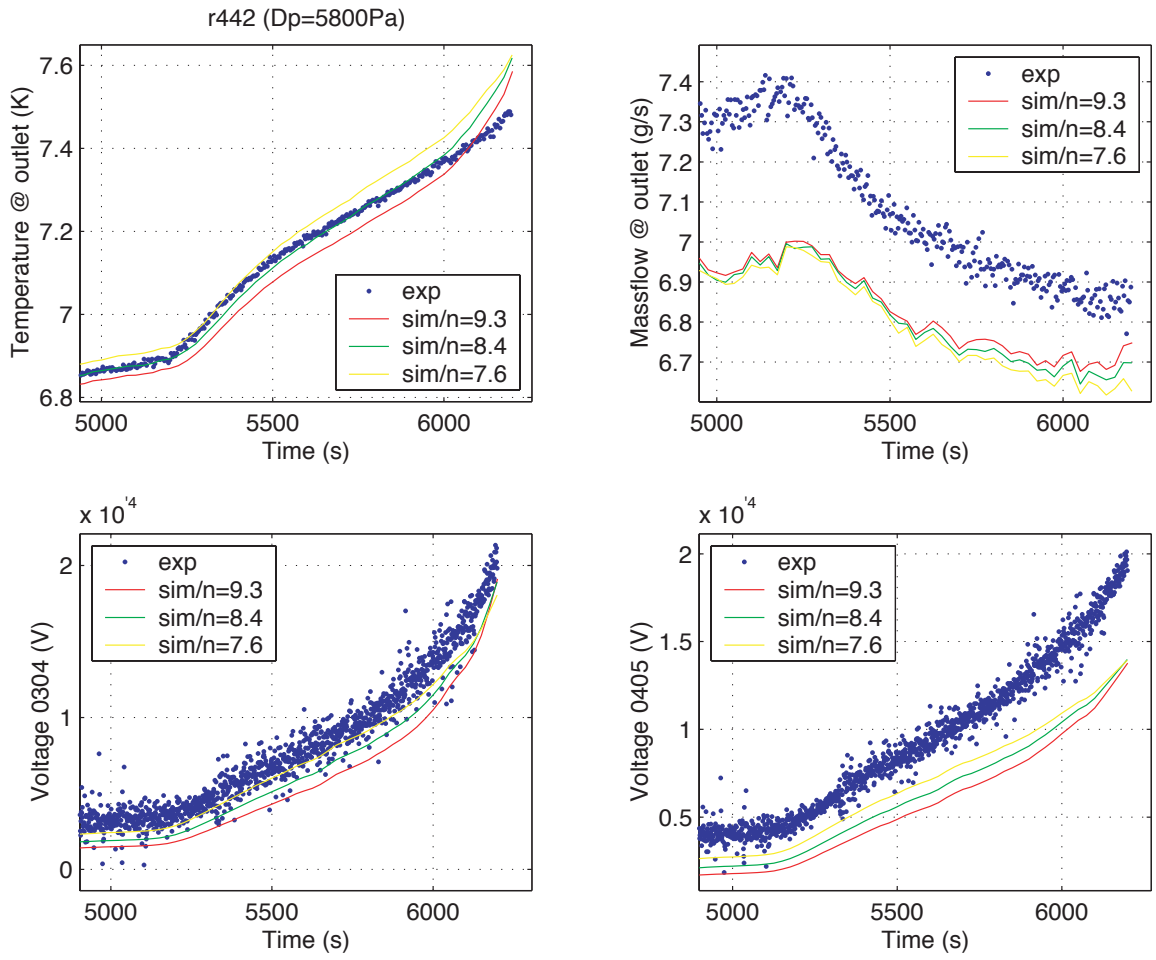

Figure E7. Sensitivity to n-value of run #44-2. Comparison between experimental (blue) and simulated (red: n = 8.6, green: n = 7.6 and yellow: n = 7.1) time history of thermal hydraulic variables and resistive voltages. Details in the final evolution of the run.

Appendix F. Sensitivity to outlet pressure correction

A limited sensitivity analysis is performed to assess the influence of the pressure correction factor C3 on the relevant results of the simulation, e.g. total strain, outlet temperature, outlet mass flow rate, resistive voltage V0304 and current sharing temperature.

The study is applied to three runs at high magnetic field (> 11.4 T) and low, medium and high TFCI current, i.e. 17.6 kA (#43-4), 31.0 kA (#40-3) and 46.0 kA (#42.2). In each run n = 7.6 and the pressure correction factor 5800 Pa < C3 < 6800 Pa.

F.1. Results

- The 'optimal' fitting parameter ε is selected after few iterations resulting in larger negative values for lower C3 values (Table F1).
- All output variables are quite insensitive to variation of C3. A summary at t = t_{end} is shown in Fig. F1.
- A decrease of C3 produces a limited decrease of temperature and mass flow rate @ the outlet whereas the voltages remain practically unchanged (Fig. F2-F7).

Run #	B_{max} (T)	I_{TFCI} (kA)	BI (kN/m)	C3 (Pa)	n (-)	ε (%)	T_{cs} (K)
Note ->							(a)
40-3	11.511	31.775	365.8	5800	7.1	-0.5890	8.22
					7.6	-0.5890	8.22
					8.6	-0.5840	8.25
43-3	11.475	17.609	202.1	5800	6.1	-0.5965	9.02
					7.3	-0.5905	9.05
					7.6	-0.5905	9.05
44-2	12.158	46.030	559.6	5800	7.6	-0.6105	6.98
					8.4	-0.6045	7.01
					9.3	-0.5995	7.04
(a) $B=B_{max}$							

Table E1. Sensitivity of simulation to pressure correction factor C3

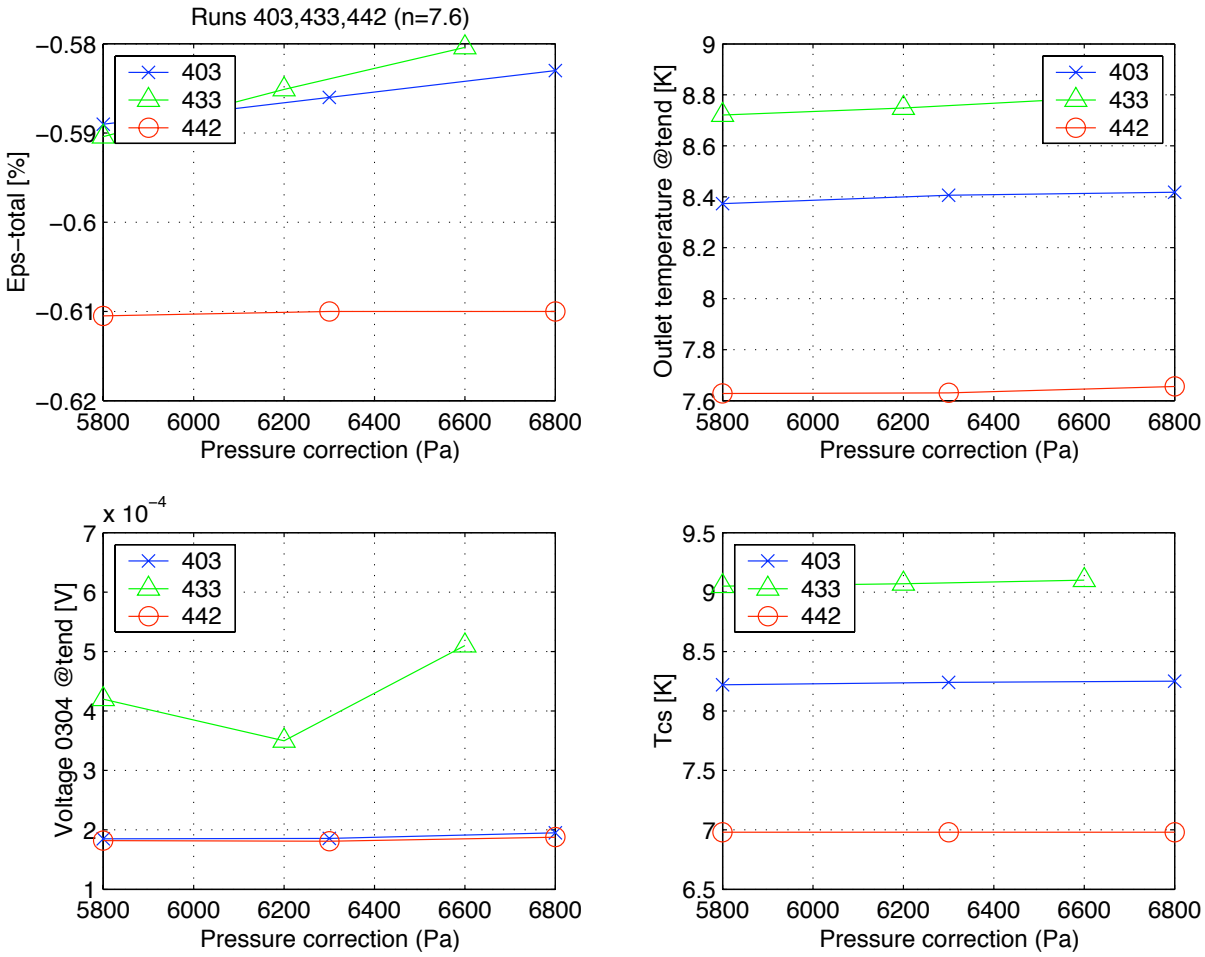

Figure F1. Sensitivity to pressure correction factor C3 of the fitting parameter ε (Eps_total), T_{cs}, outer temperature and voltage V0304 at the end of run #40-3, #43-3 and #44-2. The n-value for all runs is n = 7.6.

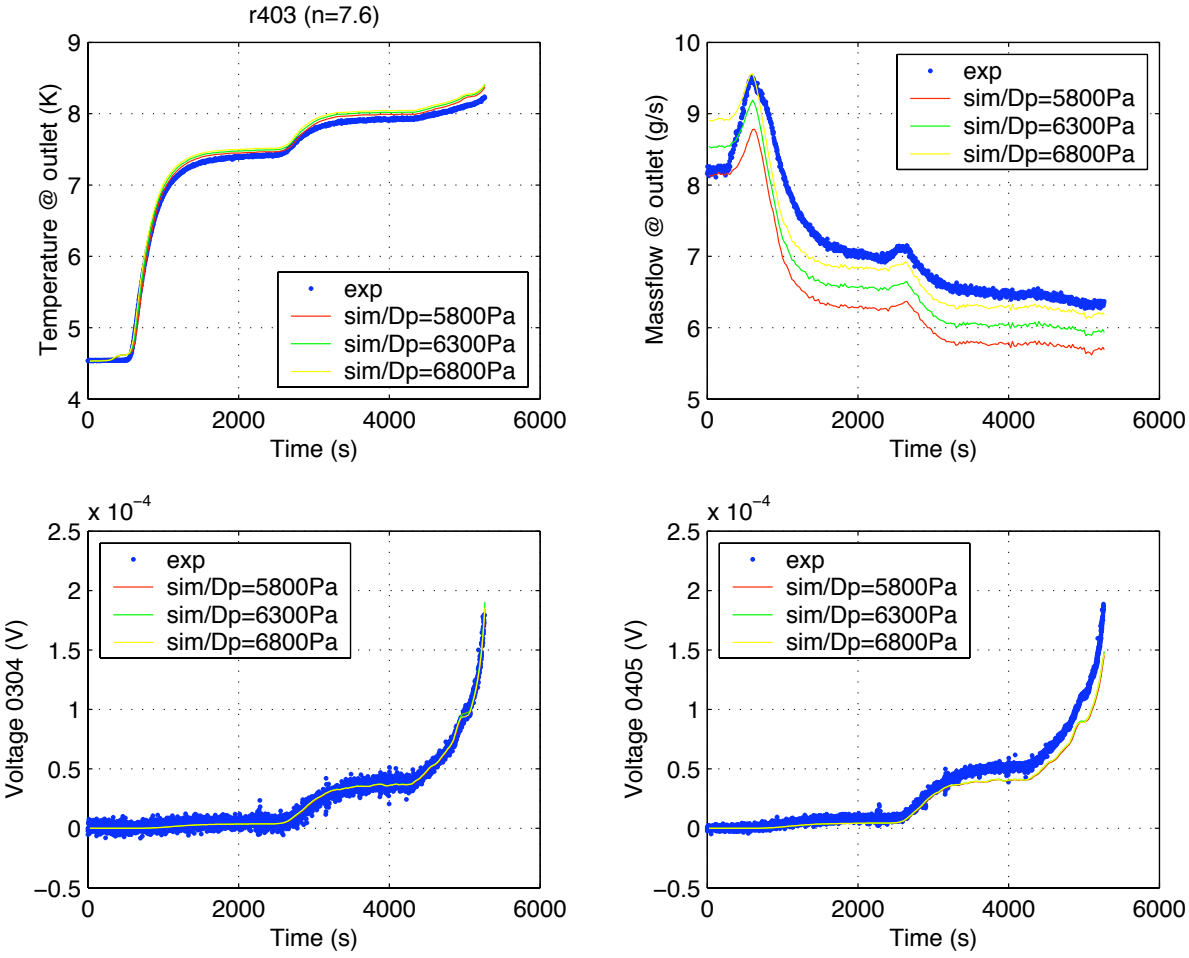

Figure F2. Sensitivity to pressure correction factor C3 of run #40-3 (n-value = 7.6). Comparison between experimental (blue) and simulated (red: C3 = 5800 Pa, green: C3 = 6300 Pa and yellow: C3 = 6800 Pa) time history of thermal hydraulic variables and resistive voltages.

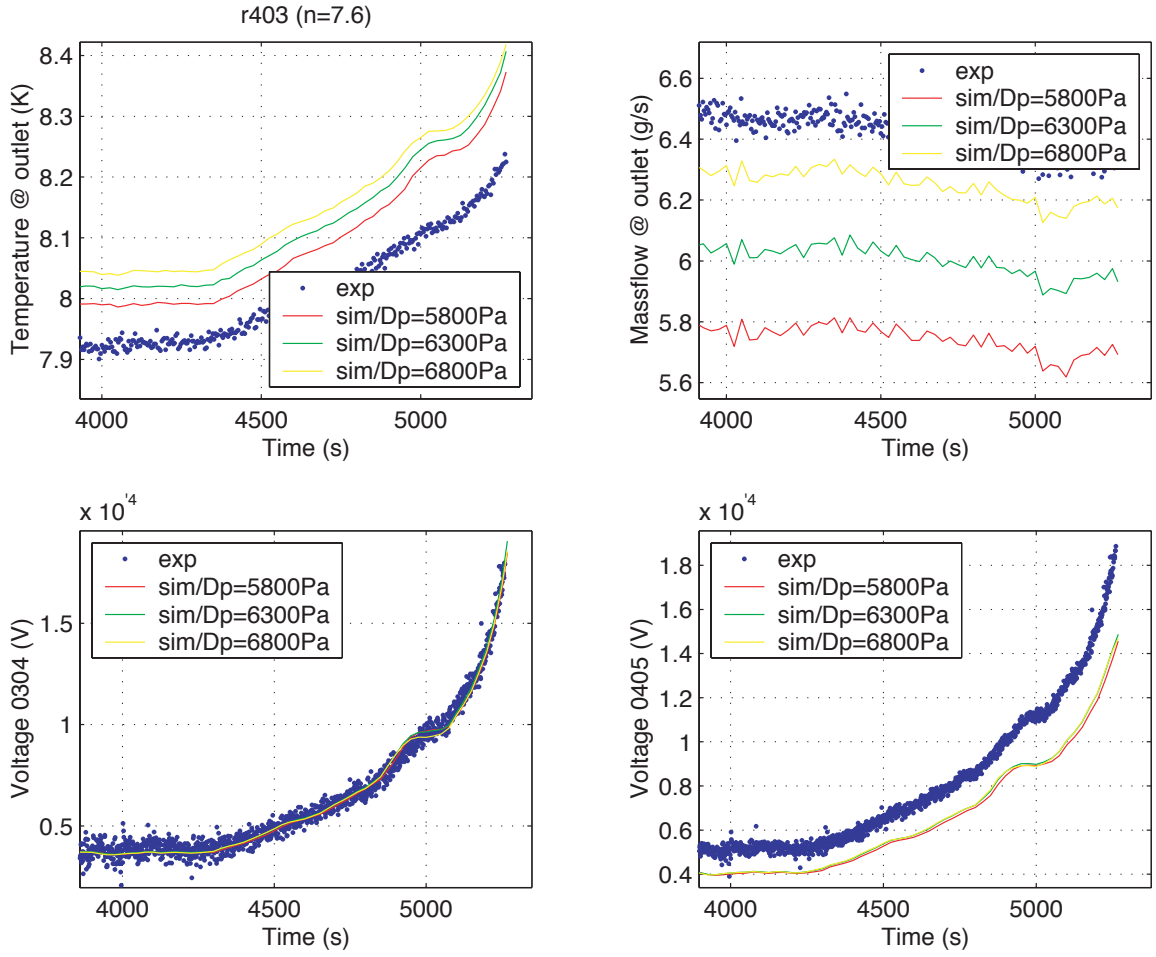

Figure F3. Sensitivity to pressure correction factor C3 of run #40-3 (n-value = 7.6). Comparison between experimental (blue) and simulated (red: C3 = 5800 Pa, green: C3 = 6300 Pa and yellow: C3 = 6800 Pa) time history of thermal hydraulic variables and resistive voltages. Details in the final evolution of the run.

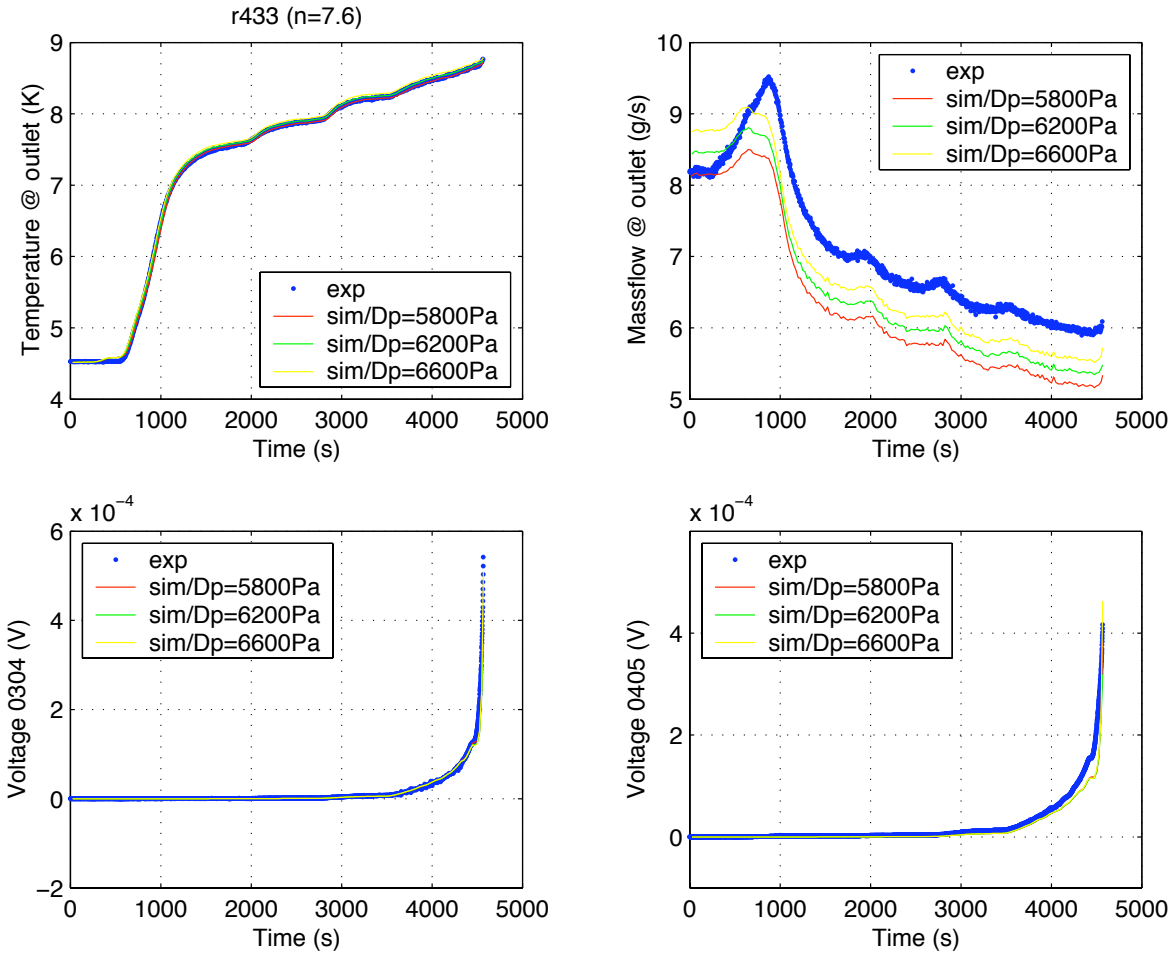

Figure F4. Sensitivity to pressure correction factor C3 of run #43-3 (n-value = 7.6). Comparison between experimental (blue) and simulated (red: C3 = 5800 Pa, green: C3 = 6300 Pa and yellow: C3 = 6800 Pa) time history of thermal hydraulic variables and resistive voltages.

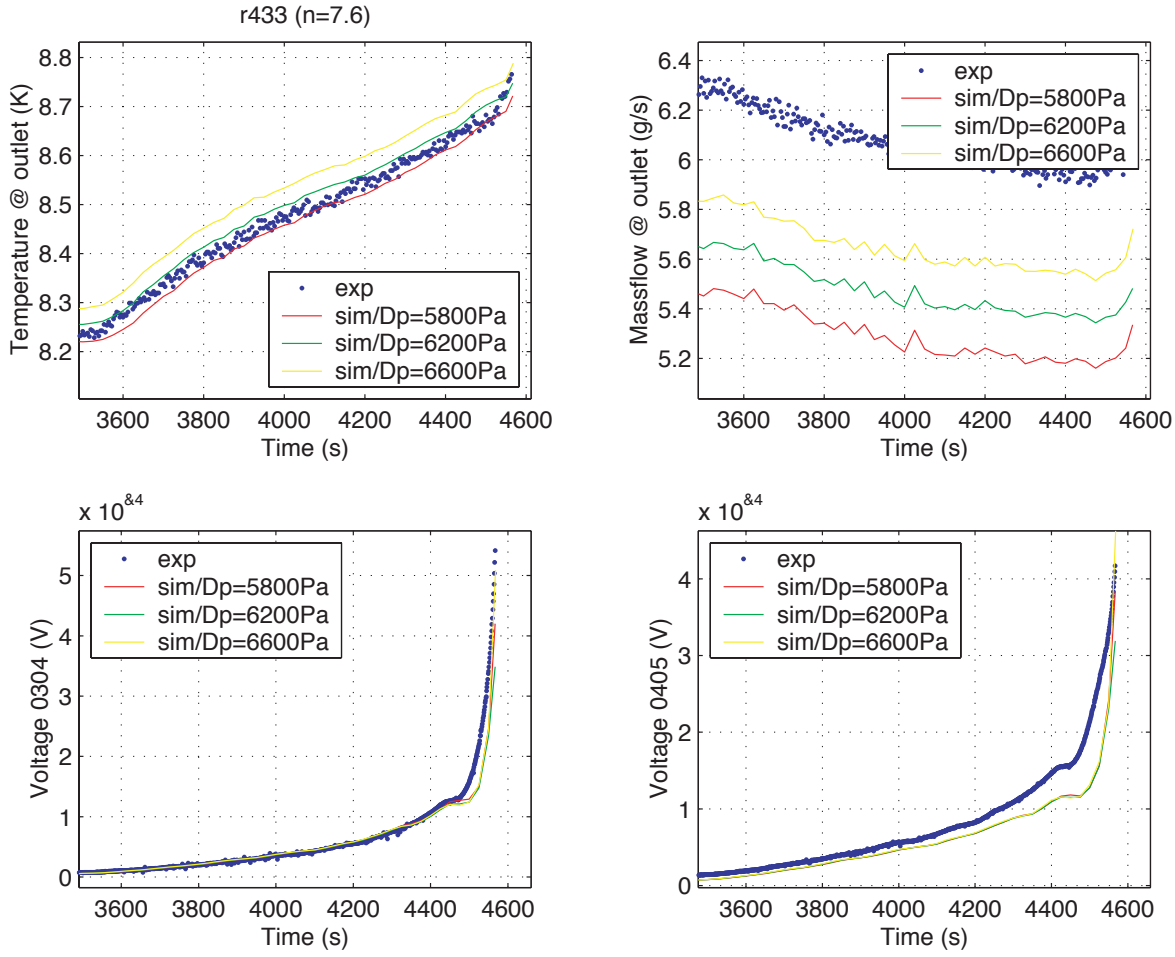

Figure F5. Sensitivity to pressure correction factor C3 of run #43-3 (n-value = 7.6). Comparison between experimental (blue) and simulated (red: C3 = 5800 Pa, green: C3 = 6300 Pa and yellow: C3 = 6800 Pa) time history of thermal hydraulic variables and resistive voltages. Details in the final evolution of the run.

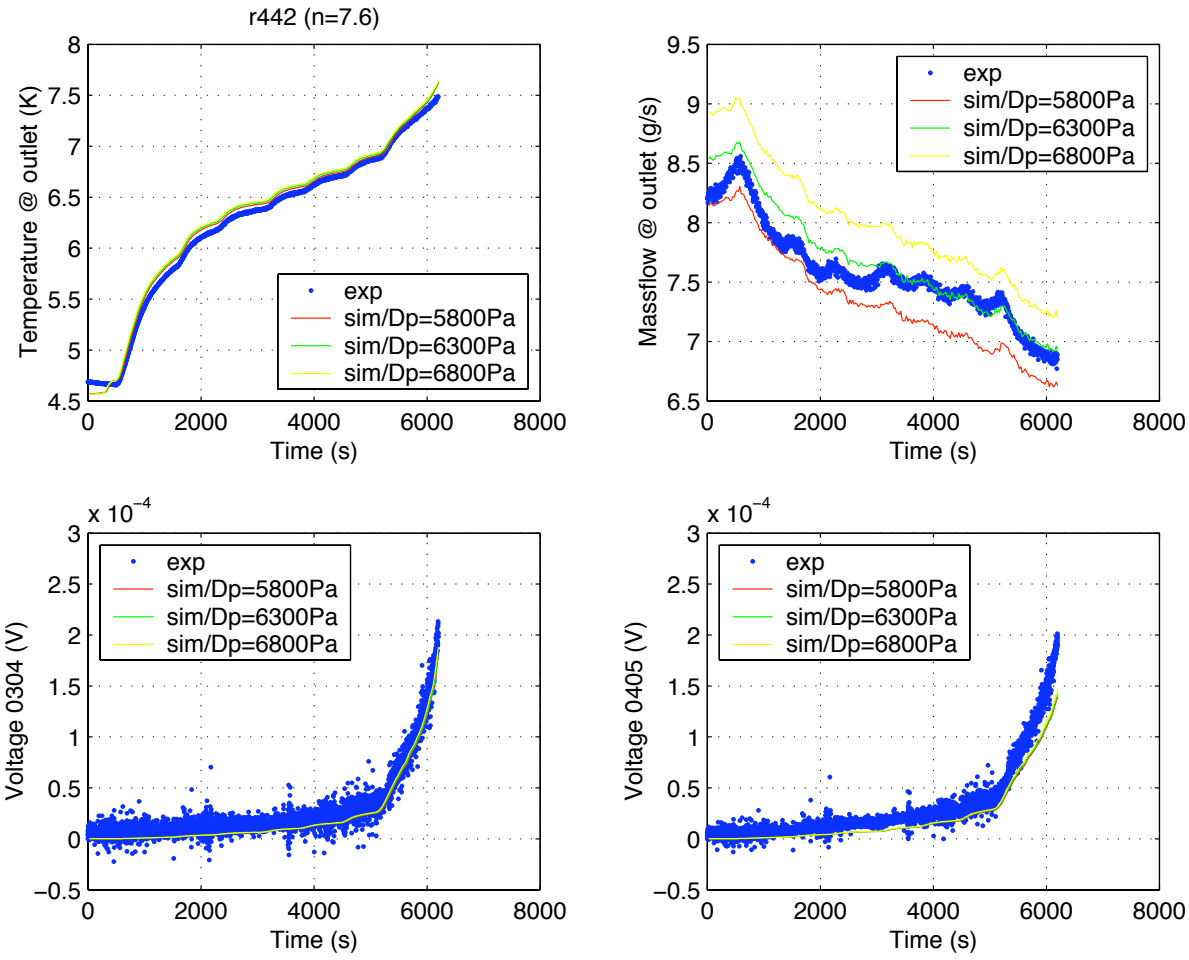

Figure F6. Sensitivity to pressure correction factor C3 of run #44-2 (n-value = 7.6). Comparison between experimental (blue) and simulated (red: C3 = 5800 Pa, green: C3 = 6300 Pa and yellow: C3 = 6800 Pa) time history of thermal hydraulic variables and resistive voltages.

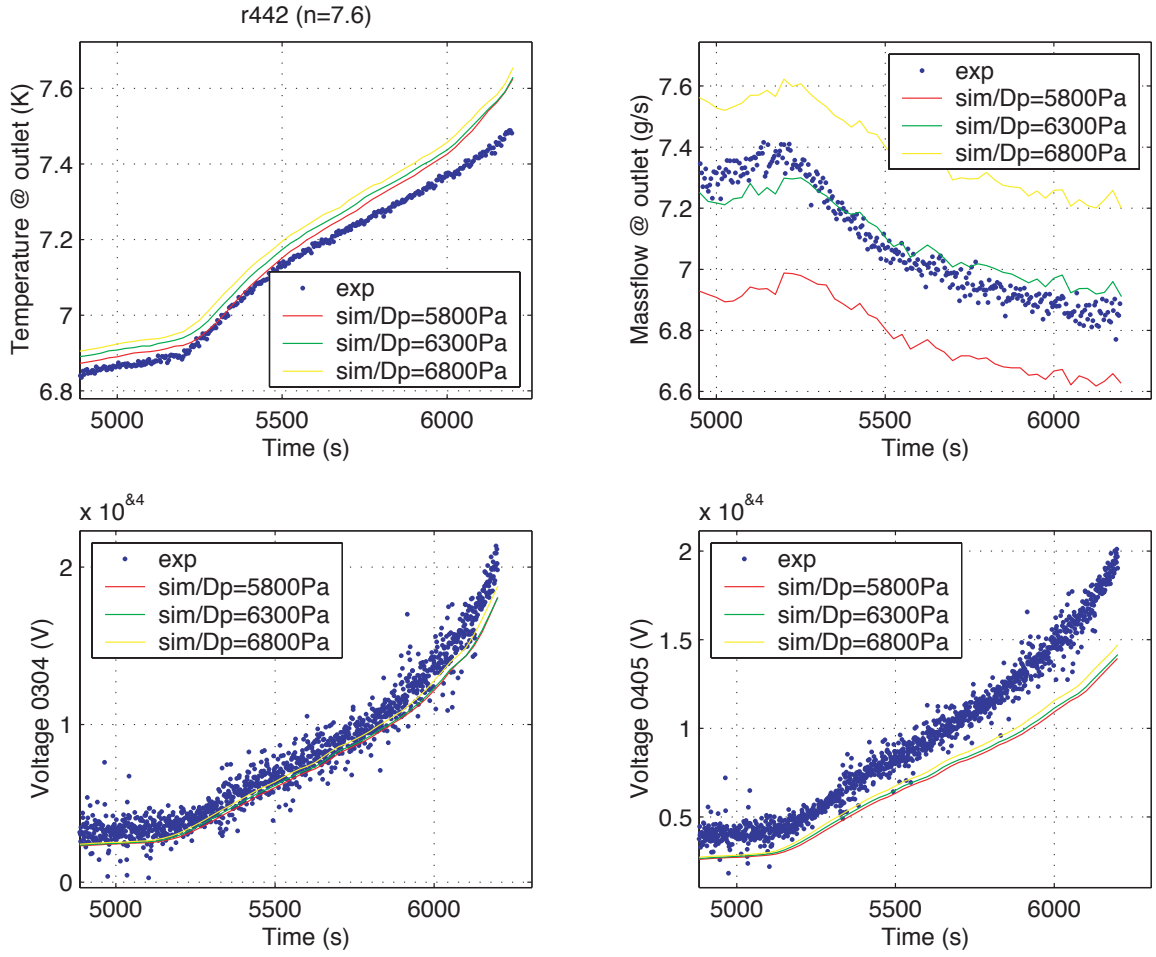

Figure F7. Sensitivity to pressure correction factor C3 of run #44-2 (n-value = 7.6). Comparison between experimental (blue) and simulated (red: C3 = 5800 Pa, green: C3 = 6300 Pa and yellow: C3 = 6800 Pa) time history of thermal hydraulic variables and resistive voltages. Details in the final evolution of the run.

Appendix G. Estimation of the cable n-values (by R. Wesche)

To simulate the thermal, hydraulic and electric behaviour of the TFCI during the T_{cs} runs the n values have to be known for the considered operating conditions, listed in Table H1.

In an I_c measurement the temperature and the magnetic field are kept constant, while the current is increased. In the region of interest the electric field-current characteristic can be described by the power law:

(1) $E(I) = E_c\,(I/I_c)^n$

where I_c is the critical current and E_c the electric field used to define I_c. Generally, the n-value is a function of field and temperature.

To measure the current sharing temperature T_{cs} the magnetic field and the current are kept constant, while the temperature is increased. The electric field-temperature characteristic can be again described by a power law, however, the exponent is different.

(2) $E(T) = E_c\,(T/T_{cs})^m$

where the exponent m depends on the magnetic field and the current. To find the n-values needed for the simulations, the E(I) curve has to be constructed using the E(T) data. The experimentally determined E(T) data provide m(B,I) and $T_{cs}(B,I)$. The E(I) curve can be calculated using the expression

(3) $E(I) = E_c\,(T/T_{cs}(B,I))^{m(B,I)}$

where T and B are constant. To obtain $n(B,T_{cs})$ the temperature $T = T_{cs}$ found from the T_{cs} measurement is selected. Due to the variation of the current $T_{cs}(B,I)$ in the denominator decreases with increasing current and the desired E(I) curve is obtained. The n-value is found by a power law fit to the calculated E(I) curve.

In a first step the experimentally determined E(T) curves were used to find the m and T_{cs} values. Because of the lack of accurate temperature measurements at the different voltage tap positions, the average of the inlet and outlet temperatures is used as a reference value. For the central turns (E0506, E0607) this assumption should provide a good approximation. On the other hand, considerably larger systematic errors in the temperature are expected to occur in the outer turns (E0304, E0405, E0708, E0809, E0910).

The m-values obtained for the central turns E0506 and E0607 are listed in Tables H2 and H3, respectively. The corresponding T_{cs} values for $E_c = 0.1\ \mu V/cm$ are presented in Tables H4 and E5.

The E(I) curves can be calculated using equation (3), when m(I) and $T_{cs}(I)$ for the considered magnetic field are known. Unfortunately, T_{cs} measurements for two different currents have been performed only at a magnetic field of 11.5 T. Assuming that m as well as Tcs depend to a first approximation linearly on the current the following expressions result for m(I) and $T_{cs}(I)$ (runs 40-3, 43-3, 63-2, 68-2)

(4) $m(I) = 81.65 - 1.395\ I$ (E0506)

(5) $m(I) = 70.50 - 1.230\ I$ (E0607)

(6) Tcs (I) = 10.31 K - 0.0625 I (E0506)

(7) Tcs(I) = 10.27 K - 0.0620 I (E0607)

where the current I is in kA. The Tcs runs at magnetic fields of approximately 12.1, 10.1 and 5.15 T have been performed only for a single value of the current. To estimate the m(I) and Tcs values for these magnetic fields it was supposed that the slopes dT_{cs}/dI and dm/dI are the same as for a magnetic field of 11.5 T. Thus, the m(I) and Tcs(I) curves for different fields are approximated by parallel straight lines.

Using equation (3) and the estimated m(I) and Tcs(I) dependencies the E(I) curves for the different B and Tcs values have been calculated. Power law fits to these E(I) curves provided the n(B,Tcs) values of the cable quoted in Table H6.

Run #	I_{TFCI} (kA)	B_{max} (T)
40-3	31.775	11.511
43-3	17.609	11.475
44-2	46.040	12.158
52-3	34.329	10.124
57-3	46.060	5.147
63-2	17.682	11.469
68-2	17.685	11.474
85-3	46.085	5.146

Table G1. TFCI T_{cs} experimental runs

B (T)	m-values					
5.146	-	-	-	-	-	48.3
5.147	-	-	-	-	-	43.4
10.124	-	-	-	44.5	-	-
11.496	-	56.1	-	-	-	-
11.474	-	53.7	-	-	-	-
11.475	61.2	-	-	-	-	-
11.511	-	-	37.3	-	-	-
~12.1	-	-	-	-	-	23.8
12.158	-	-	-	-	22.1	-
I (kA)	**17.6**	**17.7**	**31.8**	**34.3**	**46.0**	**46.1**

Table G2. m-Values obtained from E0506

B (T)	m-values					
5.146	-	-	-	-	-	37.8
5.147	-	-	-	-	-	48.2
10.124	-	-	-	41.8	-	-
11.496	-	47.8	-	-	-	-
11.474	-	47.1	-	-	-	-
11.475	51.4	-	-	-	-	-
11.511	-	-	31.4	-	-	-
12.158	-	-	-	-	19.5	-
I (kA)	**17.6**	**17.7**	**31.8**	**34.3**	**46.0**	**46.1**

Table G3. m-Values obtained from E0607

B (T)	T_{cs} (K)					
5.146	-	-	-	-	-	11.62
5.147	-	-	-	-	-	11.72
10.124	-	-	-	9.10	-	-
11.496	-	9.23	-	-	-	-
11.474	-	9.19	-	-	-	-
11.475	9.19	-	-	-	-	-
11.511	-	-	8.32	-	-	-
12.158	-	-	-	-	7.12	-
I (kA)	**17.6**	**17.7**	**31.8**	**34.3**	**46.0**	**46.1**

Table G4. T_{cs} values obtained from E0506

B (T)	T_{cs} (K)					
5.146	-	-	-	-	-	11.62
5.147	-	-	-	-	-	11.62
10.124	-	-	-	9.07	-	-
11.496	-	9.21	-	-	-	-
11.474	-	9.16	-	-	-	-
11.475	9.16	-	-	-	-	-
11.511	-	-	8.30	-	-	-
12.158	-	-	-	-	7.10	-
I (kA)	**17.6**	**17.7**	**31.8**	**34.3**	**46.0**	**46.1**

Table G5. T_{cs} values obtained from E0607

Run #	B (T)	Tcs (K)		m		n	
40-3	11.511	8.32	8.30	37.3	31.4	8.6	7.1
43-3	11.475	9.19	9.16	61.2	51.4	7.3	6.1
44-2	12.158	7.12	7.10	22.1	19.5	9.3	8.4
52-3	10.124	9.10	9.07	44.5	41.8	10.2	9.4
57-3	5.147	11.72	11.62	43.4	48.2	10.4	11.7
63-2	11.469	9.23	9.21	56.1	47.8	6.7	5.7
68-2	11.474	9.19	9.16	53.7	47.1	6.4	5.6
85-3	5.146	11.62	11.62	48.3	37.8	11.8	9.0
Voltage taps		**E0506**	**E0607**	**E0506**	**E0607**	**E0506**	**E0607**

Table G6. Estimated n-values for TFCI